THE JOURNAL OF PHYSICAL CHEMISTRY A

pubs.acs.org/JPCA Article

Modeling Hydrogen Release from Water with Borane and Alane Catalysts: A Unified Reaction Valley Approach

Sadisha Nanayakkara, Marek Freindorf, Yunwen Tao, and Elfi Kraka*

Cite This: J. Phys. Chem. A 2020, 124, 8978–8993 Read Online

ACCESS | Metrics & More | Article Recommendations | Supporting Information

ABSTRACT: The unified reaction valley approach combined with the local vibrational mode and ring puckering analysis is applied to investigate the hydrogen evolution from water in the presence of small hydrides such as BH_3, metal hydrides as AlH_3, and their derivatives. We studied a series of reactions involving BH_3, AlH_3, B_2H_6, Al_2H_6, and AlH_3BH_3 with one- and two-water molecules, considering multiple reaction paths. In addition, the influence of the aqueous medium was examined. A general reaction mechanism was identified for most of the reactions. Those that deviate could be associated with unusually high reaction barriers with no hydrogen release. The charge transfer along the reaction path suggests that a viable hydrogen release is achieved when the catalyst adopts the role of a charge donor during the chemical processes. The puckering analysis showed that twistboat and boat forms are the predominant configurations in the case of an intermediate six-membered ring formation, which influences the activation barrier. The local mode analysis was used as a tool to detect the H−H bond formation as well as to probe catalyst regenerability. Based on the correlation between the activation energy and the change in the charge separation for cleaving O−H and B(Al)−H bonds, two promising subsets of reactions could be identified along with prescriptions for lowering the reaction barrier individually with electron-donating/withdrawing substituents.

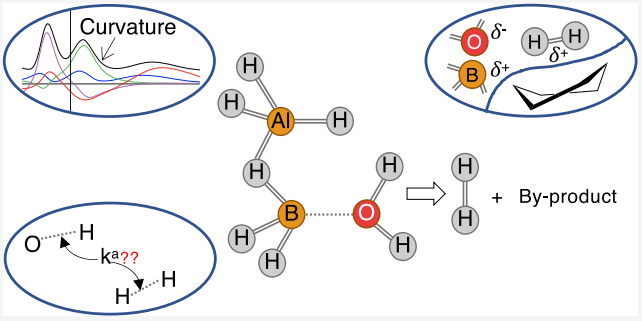

INTRODUCTION

Economic, energy-efficient, and environmentally benign hydrogen production is highly targeted in the transition from conventional fossil fuels to clean and renewable hydrogen power.[1−4] However, the intended benefits of future hydrogen economy are vastly limited by the fact that we are still relying on fossil fuels as the primary source of hydrogen production. When switching to cleaner hydrogen production methods, water splitting is a promising approach, which can be done by various methods like electrolysis, thermolysis, thermochemical reactions, and photocatalysis. There are significant efforts underway for developing techniques associated with water splitting methods to achieve energy-efficient hydrogen production, as highlighted in several reviews[5] and publications.[6−17]

Water splitting in the presence of catalysts has presented itself as a viable option to accelerate hydrogen release from water at a lower energy cost.[18] The choice of catalysts for this purpose is largely governed by the ability to form dihydrogen interactions with water. It has been shown that dihydrogen bonding[19−22] of the type $X-H^{\delta+}\cdots{}^{\delta-}H-Y$ plays an important role in hydrogen evolution from hydrogen storage systems such as borane amines and alane amines by reducing the reaction barrier.[23−26] Some other aspects to be considered for a viable hydrogen carrier, specifically rendering them as attractive systems for on-board hydrogen supply, are low molecular weight and high hydrogen content.[27] Accordingly, main-group-element hydrides like boranes and alanes have been identified as promising candidates for facilitating hydrogen release from water, as documented in several experimental[28−30] and theoretical[31] studies. For example, Nguyen and co-workers[32] investigated the catalytic effects of monomers and dimers of boranes and alanes, BH_3, AlH_3, B_2H_6, Al_2H_6, and B−Al mixed compound, AlH_3BH_3, with water. They used high-accuracy potential energy surface (PES) calculations to determine energetic parameters. In addition, they analyzed the stationary points on the PES with atom-in-molecule (AIM)[33,34] and electron localization function (ELF)[35] approaches.

While the results of this study help to evaluate the overall performance of these catalysts, more in-depth insights need a detailed mechanistic analysis, which is not only limited to energetics or stationary points on the PES but also examines the entire reaction pathway in terms of different reaction parameters. An analysis of this scope is possible through the unified reaction valley approach (URVA) of Kraka and

Received: August 7, 2020
Revised: September 30, 2020
Published: October 16, 2020

https://dx.doi.org/10.1021/acs.jpca.0c07244
J. Phys. Chem. A 2020, 124, 8978–8993

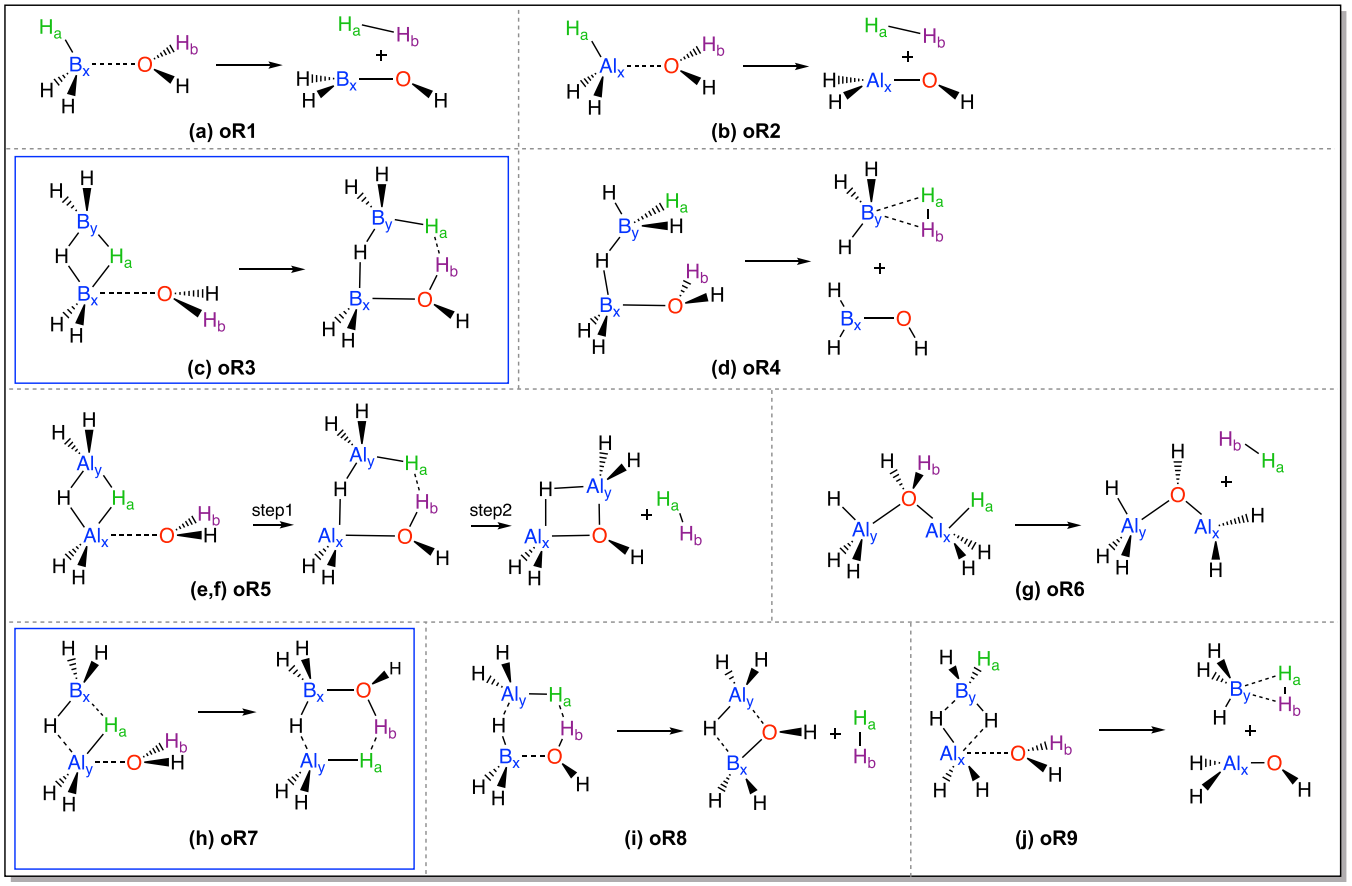

Figure 1. Reactions **oR1**−**oR9** with one-water molecule investigated in this work. Reactions shown within blue boxes represent those that do not release hydrogen during the reaction.

Cremer,[36−38] which will be described in more detail in the Computational Methods section. Mainly, our study focused on addressing the missing gaps in knowledge regarding hydrogen release by those catalysts answering questions such as: What are the major mechanistic features along the way leading to dihydrogen bond formation? What is/are driving force(s) behind these reactions?

The major objectives of this study were the following: (i) to elucidate the mechanism of hydrogen release from water, (ii) to investigate solvent effects by describing the aqueous solution using polarizable continuum model[39] (reaction $\mathbf{oR1}_{\mathbf{PCM}}$), (iii) to investigate the role of the catalyst and identify mechanistic differences between B and Al, and (iv) to derive guidelines for improving borane and alane catalysts. For this purpose, reactions **oR1**−**oR9** with one-water molecule (see Figure 1) and **tR1**−**tR12** with two-water molecules (see Figure 2) were investigated. The connection between reaction models with one- and two-water molecules is shown in Table 1.

A key distinction has to be made between all reactions, based on whether hydrogen release is accomplished during the reaction prior to understanding their reaction mechanism in depth. Reactions **oR3** and **oR7** and the two-water analogues of the latter, **tR8** and **tR9**, fall into the category (marked within the respective reaction schemes) where hydrogen release is not possible during the reaction, which deem these catalysts as unsuitable options to be used in H_2 production.

COMPUTATIONAL METHODS

The major tools applied in this work are the unified reaction valley approach (URVA)[36−38] and the local vibrational mode analysis of Konkoli and Cremer,[40−46] which will be summarized in the following text. URVA is based on analyzing the curving of the reaction path traced by the reaction complex (RC, e.g., the union of reacting molecules) on the potential energy surface (PES) from the entrance to exit channel via the TS. As the reaction proceeds, the RC undergoes electronic structure changes that are directly reflected by the scalar reaction path curvature calculated at each path point s.[38] The maxima and minima of the curvature profile can be used to retrieve significant chemical information. The curvature maxima correspond to locations where chemical events take place such as bond formation and cleavage, charge transfer, charge polarization, and rehybridization. Contrarily, the curvature minima represent locations of minimal electronic structure change, which can be associated with hidden intermediates.[47,48] A reaction phase[47,48] is defined as the path region between two minima enclosing a curvature peak. In this way, each chemical reaction is uniquely attributed with a signature pattern of curvature maxima and minima with a different number of reaction phases, i.e., a fingerprint of the reaction. Decomposition of the reaction path curvature into internal coordinate components reveals which parameter(s) dominate(s) a chemical event. A positive component supports, while a negative component resists the chemical change. For a detailed mathematical derivation and recent advances of URVA, the interested readers are referred to ref 38.

https://dx.doi.org/10.1021/acs.jpca.0c07244
J. Phys. Chem. A 2020, 124, 8978−8993

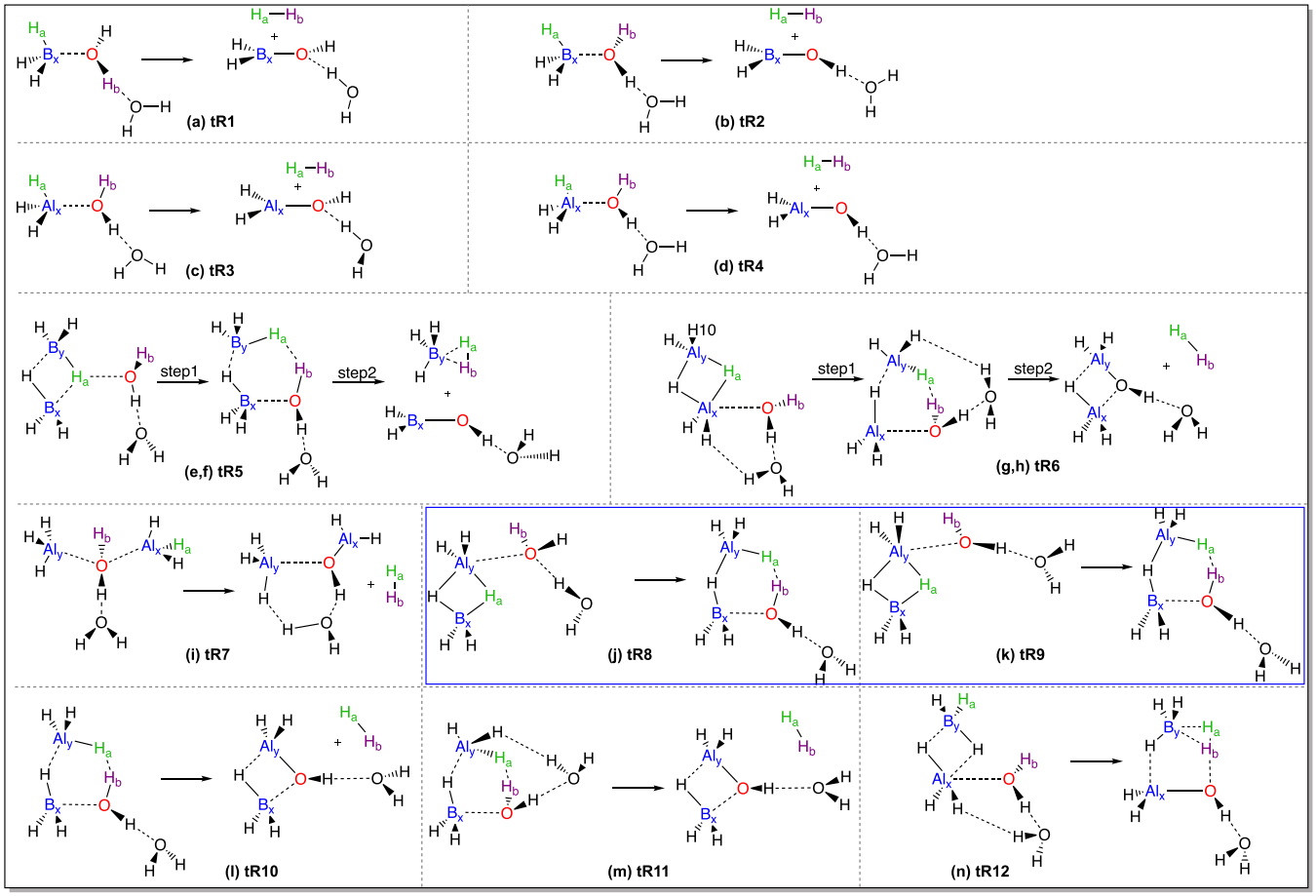

Figure 2. Reactions **tR1**−**tR12** with two-water molecules investigated in this work. Reactions shown within blue boxes represent those that do not release hydrogen during the reaction.

Table 1. Relation between Reactions Involving One-Water Molecule and Their Analogous Reactions with Two-Water Molecules Investigated in This Work

catalyst	one-water[a]	two-waters[b]
BH_3	**oR1**	**tR1**
		tR2
AlH_3	**oR2**	**tR3**
		tR4
B_2H_6	**oR3**	**tR5**, step 1
	oR4	**tR5**, step 2
Al_2H_6	**oR5**, step 1	**tR6**, step 1
	oR5, step 2	**tR6**, step 2
	oR6	**tR7**
AlH_3BH_3	**oR7**	**tR8**
		tR9
	oR8	**tR10**
		tR11
	oR9	**tR12**

[a]Reactions involving one-water molecule start with prefix **o**; [b]Reactions involving two-water molecules start with prefix **t**.

The other tool utilized in this work is the local vibrational mode analysis, which is based on vibrational spectroscopy. In particular, local vibrational force constants k^a are a quantitative measurement of the intrinsic bond strength. Local stretching force constants have been extensively applied to assess the intrinsic strength of both covalent bonding[49−63] and non-covalent[64−85] interactions. For a detailed mathematical derivation of the local vibrational mode theory, the interested readers are referred to a recent review article,[46] and recent advances involving the local vibrational mode theory can be found in refs 63 and 86.

For simplification, the local mode force constants k^a are converted into relative bond strength orders (BSOs n) by employing an extended Badger rule[48,87] according to which the BSO n is related to the local mode force constants k^a via the following power relationship[87]

$$\text{BSO } n = a(k^a)^b \tag{1}$$

The constants a and b are fully determined by the k^a values of two reference molecules with well-defined bond orders along with the requirement that for a zero-force constant, the BSO n value becomes zero. In this work, B−H and Al−H bond cleavages as well as H−H dihydrogen bond formation were investigated. For BSO n(BH), we used as reference the BH bond in BH_3 and $B_2H_7^-$, having k^a values of 4.128 and 1.901 mdyn/Å, respectively, and the corresponding Mayer bond orders[88] of 0.991 and 0.485. For BSO n(AlH), we used the AlH bonds in AlH_3 and $Al_2H_7^-$, having k^a values of 2.318 and 1.143 mdyn/Å, respectively, and the corresponding Mayer bond orders of 0.931 and 0.423. For BSO n(HH), we used the HH bond in H_2 and H_2^+, having k^a values of 6.308 and 1.740 mdyn/Å, respectively, and the corresponding Mayer bond orders of 1.000 and 0.500. For BSO n(BO), we used the BO bond in BO_2^- and BO_3^{3-}, having k^a values of 9.793 and 5.485 mdyn/Å, respectively, and

https://dx.doi.org/10.1021/acs.jpca.0c07244
J. Phys. Chem. A 2020, 124, 8978−8993

Table 2. Energetics (kcal/mol) for oR1−oR9 and tR1−tR12[a] in Gas Phase and $oR1_{PCM}$ in Solution

	MP2		DLPNO-CCSD(T)/aug-cc-pVQZ//					
	6-31+G(d,p)		MP2/6-31+G(d,p)					
Reaction	ΔE^a	ΔE_R	ΔE^a	ΔE_R	ΔH^a	ΔH_R	ΔG^a	ΔG_R
				One-Water				
oR1	24.9	−17.9	24.6	−16.2	21.7	−20.1	22.6	−24.9
oR2	17.2	−11.2	16.5	−10.0	14.3	−12.4	14.9	−17.2
oR3	25.7	12.5	24.1	10.2	23.3	10.6	28.2	15.9
oR4	9.5	−5.9	9.8	−4.1	6.7	−6.7	7.5	−11.2
oR5, step 1	5.9	0.4	5.1	0.5	4.3	−0.2	5.1	−0.3
oR5, step 2	3.6	−29.8	4.6	−27.3	2.2	−29.6	3.3	−32.8
oR6	8.8	−27.6	8.3	−29.8	5.6	−31.8	8.2	−29.8
oR7	47.5	24.1	47.4	23.0	44.1	22.1	41.7	23.5
oR8	5.1	−30.2	6.2	−27.1	3.6	−29.8	3.7	−33.5
oR9	16.9	15.5	16.4	15.0	13.3	12.9	15.2	13.4
				Two-Waters				
tR1	32.2	−10.1	32.6	−8.1	29.3	−12.3	27.7	−18.6
tR2	29.3	−13.1	29.6	−10.8	26.4	−14.9	25.8	−21.4
tR3	26.6	−3.6	26.8	−1.5	23.7	−4.7	21.8	−11.1
tR4	23.3	−3.1	23.2	−1.0	20.2	−4.1	18.8	−11.7
tR5, step 1	21.6	5.4	20.4	3.8	20.2	4.7	22.8	6.9
tR5, step 2	15.0	−1.3	15.0	0.2	11.6	−2.2	11.0	−6.1
tR6, step 1	5.2	−1.9	4.8	−1.6	3.8	−2.0	4.6	−1.2
tR6, step 2	9.9	−24.6	11.6	−20.9	9.2	−23.7	7.2	−30.8
tR7	11.9	−22.4	11.4	−23.2	8.8	−25.6	10.3	−27.7
tR8	55.5	24.6	56.2	24.2	52.6	23.3	46.9	21.6
tR9	53.1	23.7	52.9	22.7	49.8	21.9	46.7	23.4
tR10	12.8	−28.2	13.4	−25.6	10.4	−28.5	9.1	−33.3
tR11	10.6	−25.4	11.6	−22.1	8.9	−25.7	8.2	−29.5
tR12	22.0	21.8	22.3	22.1	19.3	19.9	18.8	18.2
				Aqueous Solution[b]				
$oR1_{PCM}$	30.6	−11.0	30.3	−9.4	21.67	−20.09	22.59	−24.92

[a]Activation energies ΔE^a, enthalpies ΔH^a, and free energies ΔG^a; reaction energies ΔE_R, enthalpies ΔH_R, and free energies ΔG_R. For the coupled cluster enthalpies and free energies, MP2 thermochemistry was used. [b]Using the PCM model.

the corresponding Mayer bond orders of 1.474 and 1.197. For BSO n(AlO), we used the AlO bond in AlO_2^- and AlO_3^{3-}, having k^a values of 5.326 and 2.574 mdyn/Å, respectively, and the corresponding Mayer bond orders of 1.666 and 1.150. All values refer to an MP2/6-31+G(d,p) model chemistry.[89−93]

A dual-level approach was utilized in this work, which has been proven to be effective in studying larger reaction systems in conjunction with obtaining accurate energetics.[94−97] The reaction valley was evaluated at the MP2 level with Pople's 6-31+G(d,p) basis set for all reactions **oR1−oR9** and **tR1−tR12**. The energetics were calculated at the DLPNO-CCSD(T) level of theory[98,99] utilizing MP2 geometries. The MP2 calculations were performed with a pruned ultrafine (99,590) integration grid and a tight convergence criterion. The aqueous solution applied in reaction $oR1_{PCM}$ was described by the polarizable continuum solvent model (PCM) of Tomasi and co-workers.[39] As the reaction path, the intrinsic reaction coordinate (IRC) of Fukui[100] was used with a step size of s = 0.03 amu$^{1/2}$ b, applying the improved reaction path following the algorithm of Hratchian and Kraka, enabling us to follow a chemical reaction far out into the entrance and exit channels.[101] The URVA analysis was carried out with the program pURVA,[102] and local mode analysis was carried out with the program COLOGNE20.[103] The quantum chemical calculations were performed using Gaussian09,[104] natural bond orbital (NBO) charges were calculated with the program NBO 6,[105,106] and DLPNO-CCSD(T) calculations as well as the Mayer bond order calculations were performed using the ORCA[98] program package.

RESULTS AND DISCUSSION

First, the energetics of reactions **oR1−oR9**, **tR1−tR12**, and $oR1_{PCM}$ in aqueous solution are discussed. This is followed by the URVA analysis focused on discussing the major chemical events along the reaction path of monomers, dimers, and mixed compounds of B and Al in the presence of one-water (reactions **oR1−oR9**) and two-water (reactions **tR1−tR12**) molecules. Then, a local mode analysis describing the strength of the major bonds formed and cleaved during the reactions is presented taken at the reactant (R), transition state (TS), and product (P) of each reaction. The results are complemented by an investigation of charge transfer and a ring puckering analysis.

Reaction Energetics. The activation energies and reaction energies discussed below refer to DLPNO-CCSD(T)/aug-cc-pVQZ calculations, which are summarized in Table 2. The energetics of the hydrogen release in the presence of one- and two-water molecules reveal large variations in the activation barriers, 6−47 kcal/mol for one-water, 11−56 kcal/mol for two-water. Most of the reactions involving one-water molecule are exothermic (4−30 kcal/mol) except for reactions **oR3** and **oR7** (**oR3**: 10.2 kcal/mol, **oR7**: 23.0 kcal/mol). Interestingly, **oR9** also is an endothermic reaction where H_2 is duly liberated during the reaction. The overall trend in energetics is also true for the

https://dx.doi.org/10.1021/acs.jpca.0c07244
J. Phys. Chem. A 2020, 124, 8978−8993

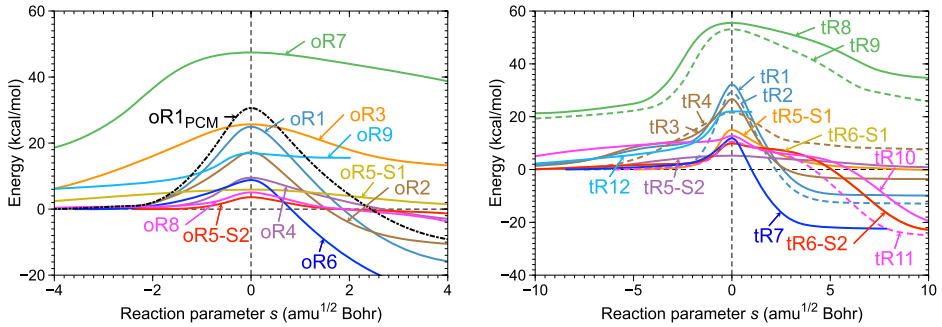

(a) **oR1-oR9** and $\mathbf{oR1_{PCM}}$ (b) **tR1-tR12**

Figure 3. Energy profiles for the (a) gas-phase reactions with one-water molecule and $\mathbf{oR1_{PCM}}$ reaction in the aqueous solution, and (b) gas-phase reactions with two-water molecules.

analogous reactions with two-water molecules, where the exothermicity is generally reduced (1−26 kcal/mol), whereas the endothermicity is increased for **tR12** (two-water analogue of **oR9**, 22.1 kcal/mol) and decreased for **tR5** (**oR3** analogue, 4.0 kcal/mol) and **tR9** (**oR7** analogue, 22.7 kcal/mol). The high activation barriers in the presence of two-water molecules are obviously a result of enhanced stabilization of the RC by hydrogen bonds in the presence of an additional water molecule. In Figure 3, the energy profiles for reactions with one- and two-water molecules in the gas phase (GP) and in aqueous solution are shown. The activation barrier in the aqueous solution (reaction $\mathbf{oR1_{PCM}}$) is increased by about 5 kcal/mol indicating that H_2 evolution is impeded in the aqueous solution.

Curvature Profiles and Reaction Mechanism. In the following, curvature profiles of **oR1**−**oR9** and **tR1**−**tR12** will be discussed with an emphasis on the mechanistic differences between reactions involving one-water molecule and their analogous reactions with an additional water molecule. Additionally, the influence of aqueous solution is analyzed via reaction $\mathbf{oR1_{PCM}}$. In Figures 4 and 5, the scalar reaction path curvatures and their decomposition into most important bond length components for these reactions are shown. Prechemical phases, which are associated with reorientations of the RC, and postchemical phases, which do not contribute to the reaction barrier, are omitted from the discussion to focus on the actual chemical events that occurred via bond formation and cleavage. Thus, the reaction path is narrowed down to only show the chemical phases. The uncurbed plots showing the entire reaction path (see Figures S3 and S4) and the respective plots for curvature decomposition into angle and dihedral components (see Figures S5−S8) are included in the Supporting Information.

An important observation is that except reactions **oR3** and **oR7**, all of the other reactions follow a similar curvature pattern within their respective chemical phases (highlighted with a gray bar). The chemical phases of these reactions (except **oR3** and **oR7**) are characterized by three curvature peaks K1, K2, and K3, recognizable as well-separated distinct peaks or small curvature enhancements in some cases. These indicate the major chemical processes of OH_b cleavage, H_aH_b formation, B_iH_a/Al_iH_a ($i = x$ for **oR1**, **oR2**, and **oR6** reactions and $i = y$ for all other reactions) cleavage, and OB_x/OAl_x formation. In all cases, the sequence of chemical events starts with the OH_b cleavage as characterized by peak K1 before the TS. This peak is dominated by the OH_b contribution accompanied by a resisting contribution from H_aH_b. In addition, K1 has small supporting contributions from OB_x/OAl_x and B_iH_a/Al_iH_a components, where the latter can also be slightly resisting in some cases.

For the majority of reactions, in the next chemical phase after the TS, the H_aH_b bond is formed as seen by the peak K2. Since H_2 formation occurs after the TS, it does not cost energy in these cases. In **oR9**, **oR5** (step 2), and **oR8**, peak K2 occurs at or slightly before TS, shifting the latter toward the exit channel leading to a late transition state. The B_iH_a/Al_iH_a bond cleavage and OB_x/OAl_x bond formation processes span throughout the entire chemical region, and the finalization of both bond cleavage and formation is achieved at peak K3 where OB_x/OAl_x shows a supporting contribution and B_iH_a/Al_iH_a can show either a small supporting or a resisting contribution. The prolonged bond cleavage of B_iH_a/Al_iH_a bonds, which expands over several peaks, closely resembles that of a metal−hydrogen bond cleavage process,[107] which is cost-effective, and it is interesting to observe a stepwise bond cleavage in the presence of nonmetallic B. As emphasized earlier, during reactions **oR3** and **oR7** (see Figure 4d,i), no hydrogen is released, i.e., there is no contribution from the H_aH_b component in the exit channel, and thus, the dominating OH_b contribution is absent in the entrance channel. These reactions are energy-demanding as evident by their curvature profiles, which reveal that the B_xH_a bond cleavage before the TS consumes energy. In comparison to the two-step reaction **oR5** with alane dimer, this unfavorable situation is circumvented by cleaving the Al_xH_a in the first step under a low-energy penalty and proceeding into the actual chemical events in the second step.

Reactions **tR1**−**tR12** are characterized by the presence of an additional water molecule. In reference to Table 2, only reactions with a reasonable activation barrier less than 25 kcal/mol as well as those leading to H_2 will be further discussed, i.e., reactions **tR4**, **tR6**, **tR7**, and **tR10**−**tR12**. The remaining reactions are included for completeness in the Supporting Information (see Figure S4).

The chemical phases for reactions with two-water molecules retain similar characteristics as in the one-water-molecule case with three curvature peaks describing the major chemical events, which are OH_b cleavage, H_aH_b formation, B_iH_a/Al_iH_a cleavage ($i = x$ for **tR4** and **tR7** reactions and $i = y$ for all of the other reactions), and OB_x/OAl_x formation. In the case of **tR6** (step 2; see Figure 5c) and **tR10** (see Figure 5e), peak K2 corresponding to the H_aH_b formation appears as a small shoulder, and in **tR12** (see Figure 5g), it becomes a small curvature enhancement. Similar to their one-water analogues, reactions **tR6** (step 2), **tR11**, and **tR12** are also associated with a late TS.

https://dx.doi.org/10.1021/acs.jpca.0c07244
J. Phys. Chem. A 2020, 124, 8978−8993

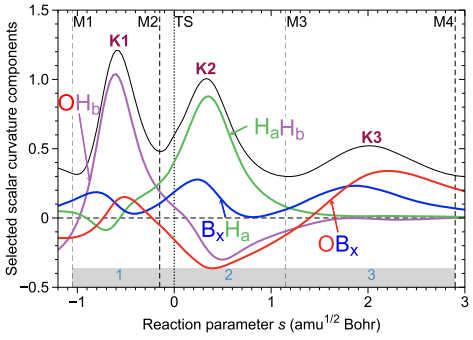

(a) Reaction **oR1, PCM**

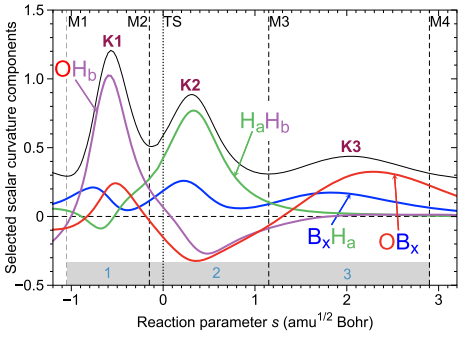

(b) Reaction **oR1**

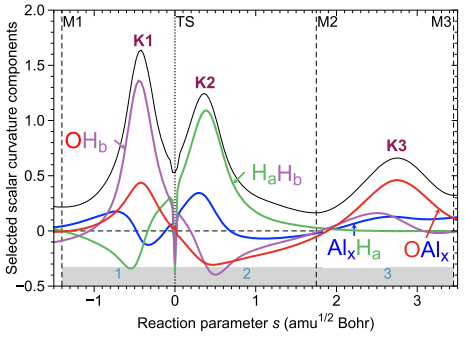

(c) Reaction **oR2**

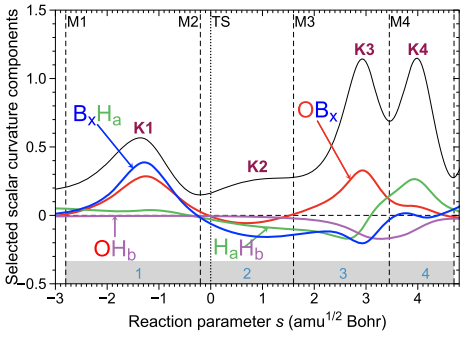

(d) Reaction **oR3**

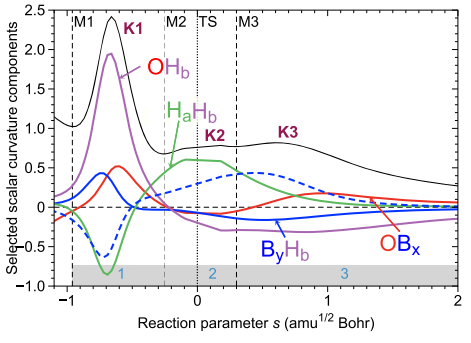

(e) Reaction **oR4**

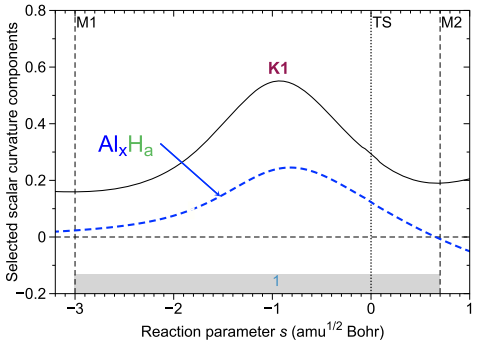

(f) Reaction **oR5**, Step 1

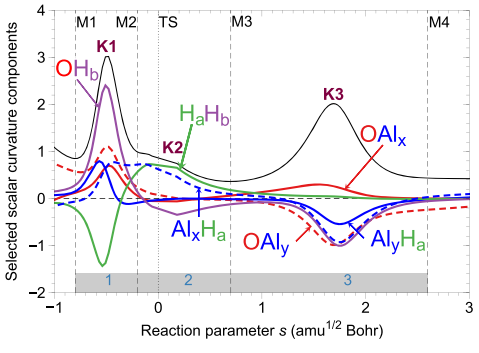

(g) Reaction **oR5**, Step 2

Figure 4. continued

https://dx.doi.org/10.1021/acs.jpca.0c07244
J. Phys. Chem. A 2020, 124, 8978−8993

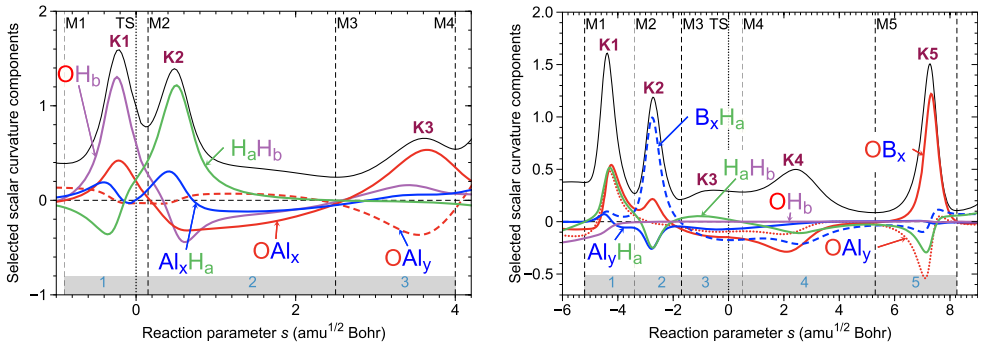

(h) Reaction **oR6** (i) Reaction **oR7**

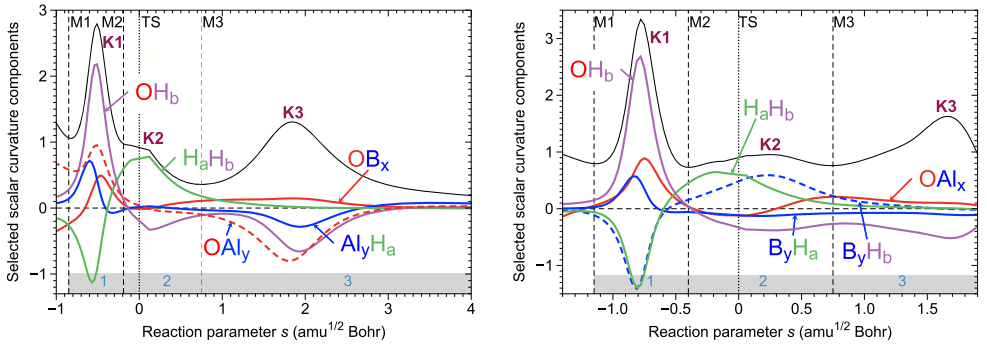

(j) Reaction **oR8** (k) Reaction **oR9**

Figure 4. Scalar curvature as a function of the reaction path parameter s (solid black line) for the hydrogen release in the presence of one-water molecule for **oR1**−**oR9** and $\mathbf{oR1}_{PCM}$ reactions in aqueous solution. The reaction path is narrowed down to show only the chemical phases (gray bar). The decomposition of the scalar curvature into the most important bond components is given. The borders of the reaction phases are indicated by the vertical dashed lines at curvature minima M1, M2, M3, etc. Curvature maxima are indicated by K1, K2, K3, etc. The TS at s = 0 amu$^{1/2}$ b is also indicated by a vertical dotted line.

In addition to the major components, there are also other components that contribute significantly to the reaction mechanism. In the two-step reactions, **oR5** and **tR6**, the first step goes through cleavage of an Al_xH_a bond that is crucial to acquire the correct orientation of the RC in order for the two reacting hydrogens to come in close contact. Also in reactions **oR5**-step 2, **oR6**, and **oR8**, along with their two-water analogues **tR6**-step 2, **tR7**, **tR10**, and **tR11**, the formation of an OAl_y interaction is observed as indicated by the subsequent peak after the chemical phase (see Figure S4 in the Supporting Information). This leads to the stabilization of the byproduct, which is reflected in the high exothermicity associated with these reactions.

Relative Bond Strength Orders. *O−H Cleavage.* As the reaction sequence starts off with the cleavage of the OH bond in all reactions except those with no hydrogen release, we investigated how the strength of the OH bond is influenced by the borane and alane catalysts. We applied the local mode analysis to examine the relative change in k^a from the R to TS, as shown in Table 3. In line with the curvature data, in **oR3** and **oR7** and their two-water analogues, the OH bond strength changes only marginally, whereas for all of the other reactions, the values vary in the range of 79−97% (see Table 3). It should be mentioned that in the two-step reactions, the OH bond cleavage takes place in the second step, accordingly showing a higher perturbation of the OH bond in the second step.

H−H Formation. As suggested by the curvature data, the H−H formation occurs slightly before or after the TS. Therefore, probing the nature of the H−H bond at the TS provides useful insights, as analyzed in Figure 6. In line with the curvature data, reactions **oR3**, **oR7**, **tR8**, and **tR9** have the weakest H−H bonds at the TS, further confirming that H_2 evolution is impossible during these reactions. All of the other reactions demonstrate moderate-to-strong H−H bonds at the TS.

Additionally, we wanted to clarify whether stabilizing electrostatic interactions between hydridic $H^{\delta-}$ from B(Al) and protonic $H^{\delta+}$ from water can contribute to the activation barrier as postulated in previous works[23−26] involving borane and alane hydrides. As k^a is able to capture all electronic and steric effects, it is an ideal measure of the strength of the stabilizing interactions within the dihydrogen bond. Although there is no direct correlation between the activation energy and k^a (see Figure 7), three trends emerge (marked within differently colored dashed ovals). The region encircled in red corresponds to the reactions with high activation energies and weak H−H bond strengths. The other two regions encircled in purple and green correspond to all of the other reactions with lower activation energies and moderate-to-strong H−H bonds. Interestingly, all reactions within the green region proceed through a six-membered cyclic TS, compared to the majority of reactions within the purple region, which have a four-membered cyclic TS except **tR10**. The distinction between the two regions most probably originates from the steric strain inherent to the four-membered cyclic TS.

B(Al)−H Cleavage. As revealed by the curvature peaks, the B(Al)−H cleavage process starts before the TS and proceeds into the subsequent phases, leading to a gradual weakening of the B(Al)−H bond for all reaction resulting in hydrogen

https://dx.doi.org/10.1021/acs.jpca.0c07244
J. Phys. Chem. A 2020, 124, 8978−8993

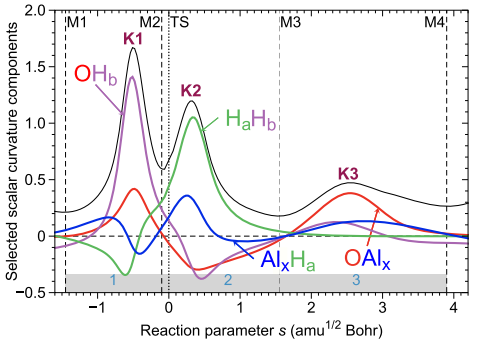

(a) Reaction **tR4**

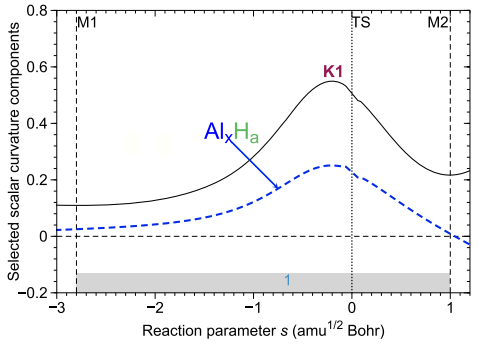

(b) Reaction **tR6**, Step 1

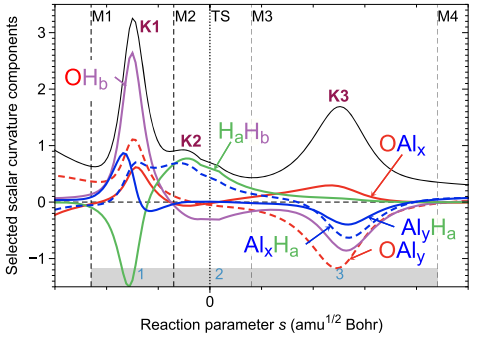

(c) Reaction **tR6**, Step 2

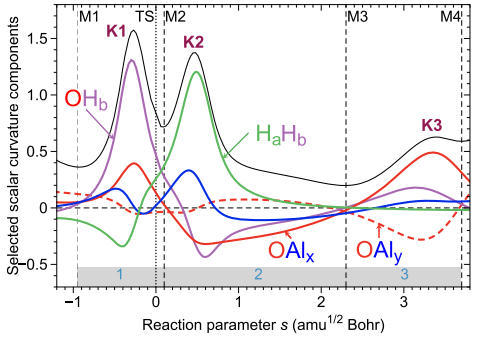

(d) Reaction **tR7**

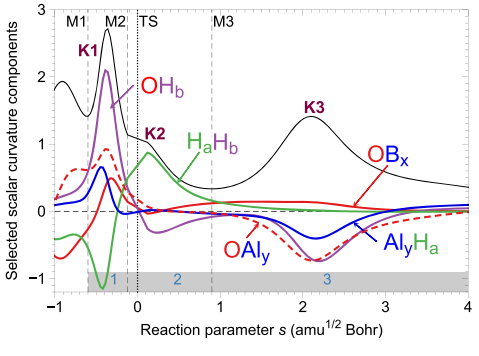

(e) Reaction **tR10**

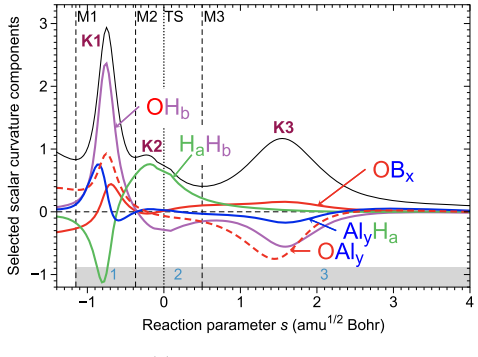

(f) Reaction **tR11**

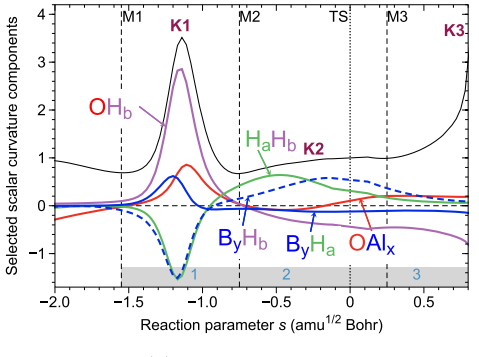

(g) Reaction **tR12**

Figure 5. Scalar curvature as a function of the reaction path parameter s (solid black line) for the hydrogen release in the presence of two-water molecules for **tR4**, **tR6**, **tR7**, and **tR10**−**tR12**. The reaction path is narrowed down to show only the chemical phases (gray bar). The decomposition of the scalar curvature into the most important bond components is given. The borders of the reaction phases are indicated by the vertical dashed lines at curvature minima M1, M2, M3, etc. Curvature maxima are indicated by K1, K2, K3, etc. The TS at $s = 0$ amu$^{1/2}$ b is also indicated by a vertical dotted line.

https://dx.doi.org/10.1021/acs.jpca.0c07244
J. Phys. Chem. A 2020, 124, 8978−8993

Table 3. Relative Change of k^a for the O−H Bond Cleavage in oR1−oR9 and tR1−tR12

reaction	k^a(**R**)[a] (mDyn/Å)	k^a(**TS**)[b] (mDyn/Å)	abs[Δk^a(%)][c]
	One-Water		
oR1	8.340	1.407	83.1
oR2	8.393	0.867	89.7
oR3	8.545	8.166	4.4
oR4	6.768	0.748	89.0
oR5, step 1	8.423	8.200	2.7
oR5, step 2	3.562	0.45	87.4
oR6	7.993	0.900	88.7
oR7	8.403	8.457	0.6
oR8	4.261	0.600	85.9
oR9	8.403	0.527	93.7
	Two-Waters		
tR1	6.482	1.344	79.3
tR2	8.380	1.411	83.2
tR3	8.448	0.873	89.7
tR4	8.448	0.783	90.7
tR5, step 1	8.590	8.221	4.3
tR5, step 2	7.632	0.479	93.7
tR6, step 1	8.452	8.439	0.2
tR6, step 2	6.102	0.454	92.6
tR7	8.068	0.933	88.4
tR8	8.516	8.152	4.3
tR9	8.407	8.543	1.6
tR10	5.733	0.395	93.1
tR11	6.698	0.488	92.7
tR12	8.451	0.285	96.6

[a]Local mode force constant for the R. [b]Local mode force constant for the TS. [c]The absolute change of force constant from the R to TS as a percentage.

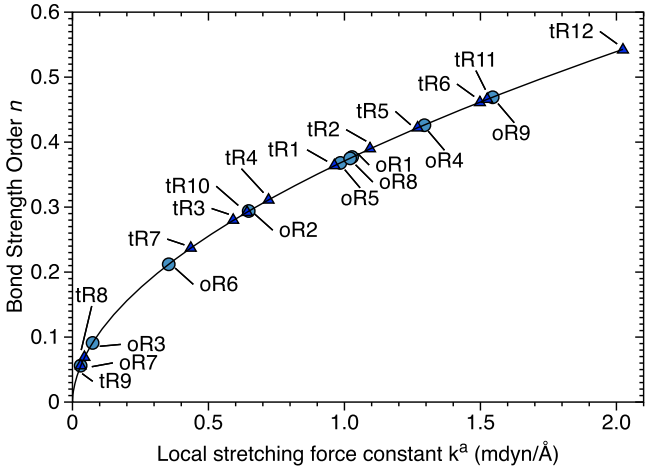

Figure 6. Power relationship between the BSO n and k^a values for H−H bonds at the TS for reactions with one-water (blue circles) and two-water (dark blue triangles) molecules.

evolution. This process is analyzed via the BSO n values determined at the R, TS, and P, as shown in Figure 8. Since BSO n values were determined using two different power relationships for B−H (solid curve) and Al−H (dashed curve) bonds, the corresponding data points are separated into their respective curves. In the R (red points), B−H bonds appear to be generally stronger than Al−H bonds with BSO n values between 0.8 and 1.0. The BSO n values decrease at the TS (blue points) but still remain moderately strong with values between 0.4 and 0.6,

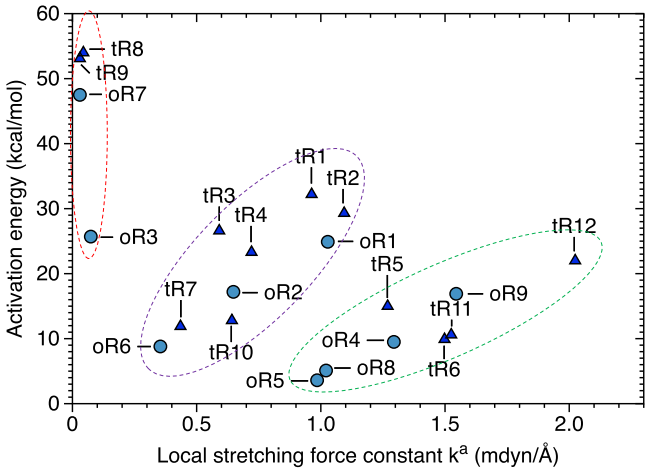

Figure 7. Correlation between the activation energy and k^a values for H−H bonds at the TS for reactions with one-water (blue circles) and two-water (dark blue triangles) molecules.

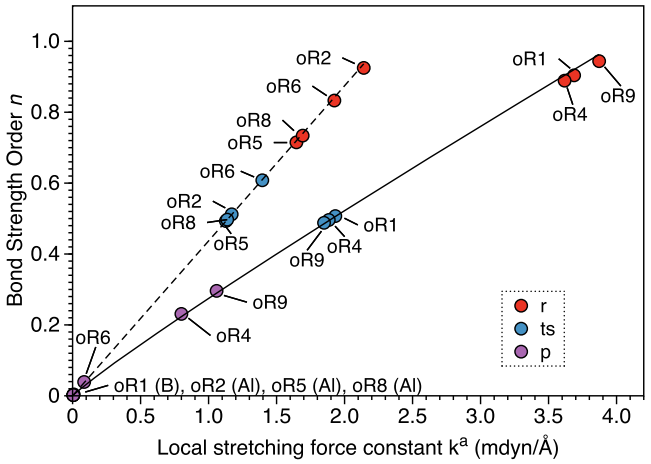

Figure 8. Power relationship between the BSO n and k^a values for B−H and Al−H bonds at R, TS, and P. Unless otherwise stated (in parentheses), the solid and dashed curves represent the B−H and Al−H bonds, respectively.

indicating that the bond cleavage has not been finalized yet. In the P (purple points), all except **oR4** and **oR9** have BSO n values close to zero, those with marginally strong B−H bonds implying a weak B−H interaction in the P. A similar analysis was done for reactions with two-water molecules and is included within the Supporting Information along with local mode properties at R, TS, and P for all reactions (see Figure S10 and Tables S1 and S2).

O−B(Al) Formation. A critical consideration in the catalytic H_2 production is the regeneration of the catalyst from the borate and aluminate byproducts, which is required to close the hydrogen cycle. This is very challenging due to the inefficiency in the process of breaking an O−B(Al) bond in the byproduct to generate a B−H bond.[108−110] Utilizing the local mode analysis to inspect the intrinsic bond strength of O−B(Al) bond(s) in the byproduct, we were able to shed some new light on the regenerability of the catalyst, which is a complex process and a comprehensive analysis is required, however, to further understand its proper mechanism.

As seen from Figure 9, the strongest O−B(Al) bonds are formed in the byproducts from the reactions **oR1**, **oR2**, **oR4**,

https://dx.doi.org/10.1021/acs.jpca.0c07244
J. Phys. Chem. A 2020, 124, 8978−8993

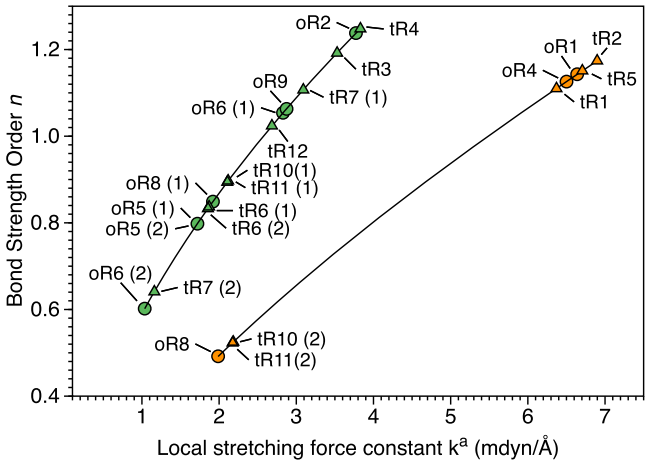

Figure 9. Power relationship between the BSO *n* and k^a values for B−O (in orange) and Al−O (in green) bonds in the P, for complete reactions with one-water (circles) and two-water (triangles) molecules. In the case of multiple O−B(Al) bonds, they are shown by numbers in parentheses.

oR6, and **oR9** and their two-water analogues **tR1**−**tR5**, **tR7**, and **tR12**, having BSO *n* values between 1.0 and 1.3. Reactions **oR6** and **tR7** lead to relatively weak secondary (numbered as 2, BSO *n*: 0.6) Al−O bonds; however, having strong primary (numbered as 1, BSO *n*: 1.1) Al−O bonds restricts the efficiency of these byproducts in the regeneration process. Interestingly, the byproducts from reaction **oR8** along with its two-water analogues **tR10** and **tR11** emerge to have very weak B−O bonds (BSO *n*: 0.5), in addition to moderately strong primary Al−O bonds (BSO *n*: 0.8−0.9), rendering it as a desirable candidate to be considered for catalyst regeneration. In addition, similar to the B(Al)−H cleavage, the O−B(Al) formation also follows a stepwise procedure with moderately strong O−B(Al) bonds at the TS (see Tables S3 and S4 of the Supporting Information).

Charge Transfer. We performed an NBO charge analysis along the reaction path, as shown in Figure 10, for the catalyst (Figure 10a,b) and the two hydrogen atoms (Figure 10c,d) taking part in the dihydrogen bond.

We observed that the charge transfer starts already in the van der Waals region, i.e., in the entrance channel, where the catalyst accepts charge from water in all reactions involving one- and two-water molecules. In the case of one-water molecule, the net charge acquired by the catalyst in the beginning goes to a maximum of 300 m*e*, and in the two-water case 334 m*e*. It seems that the introduction of a second water molecule to the initial RC has little influence on the charge-transfer process, which primarily occurs between the catalyst and the water molecule in direct contact. After passing through a minimum (see the dip in the curves in Figure 10a,b), the charge transfer switches direction before the TS for the majority of the reactions, revealing the bifunctional nature of borane and alane catalysts. It should be mentioned that in the first step of **oR5** and similarly in **tR6**, the charge-transfer switching point is observed after the TS, but in both cases, the major chemical events occur in step 2. However, **oR3** and **oR7** and their two-water analogues **tR8** and **tR9** are in contrary where they continue to act as charge acceptors as the reaction proceeds.

After switching direction, the catalyst starts to act as a charge donor with the above-mentioned exceptions, and for the majority of the reactions, it is observed that the net charge donated reaches a maximum during the chemical phases corresponding to the OH cleavage and HH formation. In fact, the highest charge donated within the chemical phases varies between 70 and 470 m*e* in the one-water scenario and 60−700 m*e* with two-water molecules. In all reactions where the catalyst acts as a charge donor in the chemical phases, an energy barrier of around 5−25 kcal/mol is observed with one-water molecule and 10−30 kcal/mol for two-water molecules. This increases up to 55 kcal/mol in the cases where the catalyst reverses its role and acts as a charge acceptor in the chemical phases. This is an indication that the preferred role for the catalyst is as a charge donor for a feasible hydrogen release.

We further analyzed in reaction **oR3** the inability to act as a donor, in comparison to **oR5** reaction where the catalyst is bifunctional, via a molecular orbital approach as provided by the NBO analysis. It was seen in **oR3**, initially, that the electron density of the s-orbital in the bridged H_a atom is delocalized into nonbonding p orbitals of both B_x and B_y, as suggested by the strong interaction energies (second-order perturbation energies, *E*2: 817 and 878 kcal/mol). Meanwhile, the electron acceptor ability from the lone pair of the incoming O atom into the nonbonding p-orbital of B_x is greatly reduced (*E*2: 0.85 kcal/mol). As the reaction proceeds from the R to TS, the acceptor ability of the latter increases (*E*2: 142 kcal/mol), but the electron donor capacity from the B_y−H_a sigma bond into the O−H_b sigma antibonding orbital remains very low (*E*2: 0.25 kcal/mol), consequently restricting the O−H_b bond cleavage and B_y−H_a sigma and H_b s-orbital overlap that need to promote the dihydrogen interaction. In contrast, in **oR5**, the nonbonding p-orbital of Al_x strongly accepts electron density from the O lone pair in the beginning (*E*2: 48 kcal/mol), and going toward the TS, the Al_y−H_a sigma bond weakly donates (*E*2: 0.84 kcal/mol) to the O−H_b sigma antibonding orbital, which substantially increases (*E*2: 45 kcal/mol) in the intermediate after the first step, thereby promoting OH bond cleavage in the second step and subsequent H_2 formation.

In addition, the charges on the two hydrogen atoms, H_a from catalyst and H_b from water, were analyzed as indicated in Figure 10c,d. It can be seen that H_a in the catalyst is more negatively charged than H_b in water in the beginning, and the charge on both H atoms deteriorates rapidly after TS, in all complete reactions as the H_a−H_b bond is formed. The electrostatic attractions between the oppositely charged H atoms drive the H−H bond formation process, which is, however, unattainable in **oR3** and **oR7** and the two-water analogues of the latter, **tR8** and **tR9**.

Considering the reaction in the aqueous solution, $\mathbf{oR1}_{PCM}$ (see Figure 10e), it can be seen that shortly before the TS, the catalyst changes the charge-transfer direction and proceeds as a charge donor, donating a maximum of 655 m*e*. Altogether, the charge-transfer mechanism seems more or less similar to its gas-phase counterpart. However, in comparison to **oR1**, the charge separation between the catalyst and water in the van der Waals complex appears to be higher, which is a consequence of the polar medium.

As charge transfer is a crucial factor in the reaction mechanism, we were interested in deriving an explicit relationship between the charge-transfer process and the activation energy ΔE^a. By taking into account that O−H and X−H (X = B, Al) bond cleavage processes occur or in the case of the latter initiates before the TS and these cost energy, it was worth analyzing how the change in the charge separation, going from the R to TS for the respective atoms of the cleaving bond, i.e., charge separation between the O and H atoms for the O−H

https://dx.doi.org/10.1021/acs.jpca.0c07244
J. Phys. Chem. A 2020, 124, 8978−8993

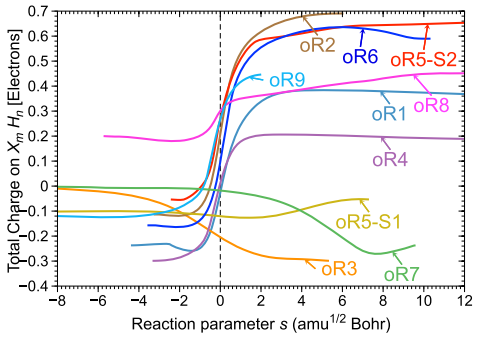

(a) Total NBO charge on catalyst X_mH_n (X=B, Al) for **oR1-oR9**

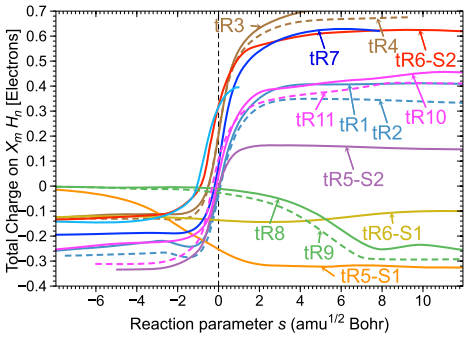

(b) Total NBO charge on catalyst X_mH_n (X=B, Al, B-Al) for **tR1-tR12**

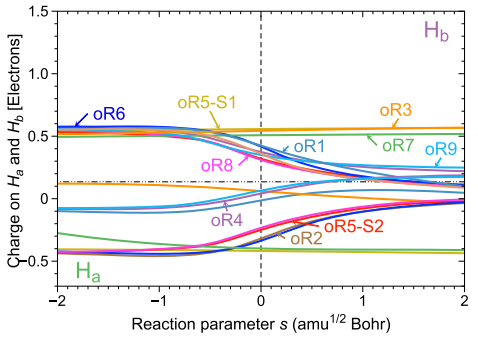

(c) Partial NBO charge on H_a and H_b for **oR1-oR9**

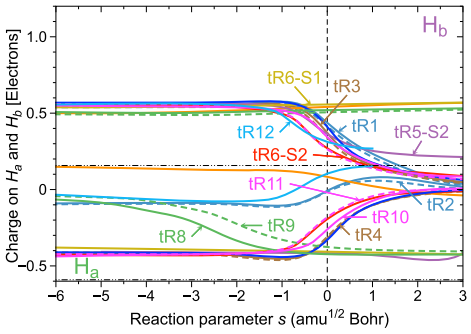

(d) Partial NBO charge on H_a and H_b for **tR1-tR12**

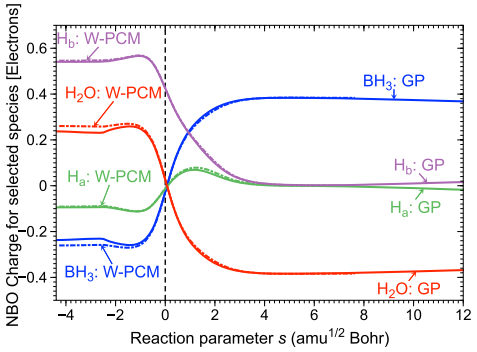

(e) Total NBO charge on catalyst BH_3 and water, and partial NBO charge on H_a and H_b for $\mathbf{oR1_{PCM}}$

Figure 10. NBO charges as a function of the reaction parameter s on (a, b) catalyst and (c, d) hydrogen atoms from the catalyst (H_a) and water (H_b), for reactions **oR1**−**oR9** with one-water molecule and **tR1**−**tR12** with two-water molecules. The dashed horizontal line separates H_a and H_b, which corresponds to the lower and upper parts of the graph, respectively. (e) Total NBO charge on the catalyst and water, and partial NBO charge on H_a (catalyst) and H_b (water) for $\mathbf{oR1_{PCM}}$. The solid lines indicate the gas-phase (GP) reaction **oR1**, and the dashed lines indicate the aqueous-phase (W-PCM) reaction $\mathbf{oR1_{PCM}}$. The TS at s = 0 amu$^{1/2}$ b is indicated by a vertical dotted line.

bond and between the X and H atoms for the X−H bond, correlates with the ΔE^a. It was immediately observed that there is a distinct division in the data set based on the predominant type of correlation as shown by Figure 10 for reactions **oR1**−**oR9**. For reactions **oR1**, **oR2**, **oR4**, and **oR8**, there is an inverse relationship with ΔE^a for the cleaving O−H bond where a small change in the charge separation between the O and H atoms going from the R to TS results in a higher ΔE^a (see Figure 11a). In contrast, reactions **oR3**, **oR5**, **oR6**, **oR7**, and **oR9** show a direct correlation with the change in charge separation for the cleaving X−H bond where a large charge separation in the X−H bond as it goes from the R to TS leads to a higher ΔE^a (see Figure 11b). For each of the reactions, by considering the predominant O−H or X−H contribution to the ΔE^a and its nature, one can derive useful guidelines to modify the catalysts so that the ΔE^a is reduced. In the cases of **oR1**, **oR2**, **oR4**, and **oR8**, electron-withdrawing substituents on the catalyst will result in higher charge separation for the O−H bond, thereby reducing the ΔE^a. Likewise, electron-donating substituents in the cases of **oR3**, **oR5**, **oR6**, **oR7**, and **oR9** can reduce the charge separation in the X−H bond and lead to lower ΔE^a. An analysis of similar nature was conducted for the two-water case, which shows parallel trends and is included in the Supporting Information (see Figure S9).

https://dx.doi.org/10.1021/acs.jpca.0c07244
J. Phys. Chem. A 2020, 124, 8978−8993

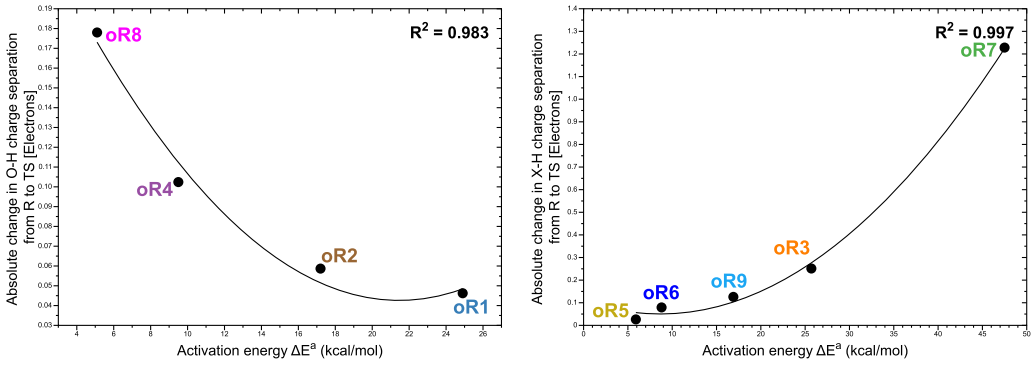

(a) Correlation between activation energy ΔE^a and absolute change in the charge separation between O and H atoms in the cleaving OH bond going from the R to TS

(b) Correlation between activation energy ΔE^a and absolute change in the charge separation between X (X=B, Al) and H atoms in the cleaving XH bond going from the R to TS

Figure 11. Correlations between the activation energy ΔE^a and the cleaving OH and XH (X = B, Al) bonds for reactions **oR1**−**oR9**.

Puckering Analysis. It has been shown in previous studies that the catalyst actively participates in the hydrogen transfer through a six-membered cyclic TS,[32] which has been observed for several reactions in this study. However, a quantitative measurement of the ring puckering and its influence on the hydrogen transfer mechanism has not been discussed so far. We used the Cremer−Pople puckering analysis[111−113] to evaluate the puckering of the intermediate six-membered rings, which is discussed in detail in the following.

The Cremer−Pople puckering analysis probes the conformational changes in the RC during the reaction and provides a quantitative description of the intermediate rings. The puckering analysis for a six-membered ring is based on the following parameters: puckering amplitudes q_2 and q_3, the pseudo-rotation phase angle Φ_2, the hyperspherical angle Θ, and the total puckering amplitude Q. The combination of the pseudo-rotational coordinate pair (q_2, Φ_2) describes the pseudo-rotation of the boat and twistboat forms of the six-membered ring, while the single-crown puckering amplitude (q_3) describes the chair (positive q_3) and inverted chair forms (negative q_3). The contributions from each of the conformations, chair, boat, and twistboat forms, can be quantified using the values of the puckering coordinates as given by the following formulas[111−113]

$$\text{chair: } 100\% \times \frac{q_3^2}{Q^2} \tag{2}$$

$$\text{boat: } 100\% \times \frac{q_2^2}{Q^2}\cos^2(3\Phi_2) \tag{3}$$

$$\text{twistboat: } 100\% \times [1 - \cos^2(3\Phi_2)]\frac{q_2^2}{Q^2} \tag{4}$$

In Table 4, the percentage contribution from each of the chair, boat, and twistboat conformers is summarized for the TS of reactions involving a six-membered ring, which are **oR3**−**oR5** and **oR7**−**oR9** and their two-water analogous reactions **tR5**, **tR6**, and **tR8**−**tR12**. According to the puckering analysis, the TS of the majority of the reactions has a predominant twistboat character, the contributions varying from 36 to 93%. The transition state of reactions **oR3** and **oR4** along with **tR8**, **tR10**, and **tR11** is predominated by the boat form with contributions 73.8, 86.5, 47.4, 66.5, and 56.6%, respectively.

Table 4. Puckering Analysis for the TS Involving a Six-Membered Ring Formation (% Contributions)

reaction	chair	boat	twistboat
	One-Water		
oR3	15.8	73.8	10.4
oR4	12.4	86.5	1.0
oR5, step 2	14.0	0.1	85.9
oR7	27.5	6.6	65.9
oR8	8.1	23.9	68.1
oR9	42.5	3.1	54.4
	Two-Waters		
tR5, step 2	9.0	0.9	90.1
tR6, step 2	11.9	2.4	85.6
tR8	28.0	47.4	24.6
tR9	28.7	34.9	36.3
tR10	18.5	66.5	15.0
tR11	9.4	56.6	34.0
tR12	36.9	19.2	43.9

We further analyzed how the character of the TS could influence the activation barrier, as presented in Figure 12. A quadratic relationship was observed between the percentage of the twistboat character in the TS and the activation energy for the set of reactions shown in Figure 12a. It can be deduced from this correlation that a twistboat character of 70−75% would ideally be suitable for lowering the activation barrier, and in this connection, the TS of **oR8** has the most favorable conformation. For the remaining set of reactions, we could observe a quadratic relationship between an admixture of boat and twistboat characters in the TS and the activation barrier, as shown in Figure 12b. Higher admixture percentages contributed to lower activation barriers, with the TS character in **tR11** being the most favorable.

CONCLUSIONS

In this work, we probed the mechanistic features of the hydrogen evolution reaction from water in the presence of small hydrides such as boranes and alanes, in the gas phase and in solution, by employing URVA complemented with the local mode analysis and the ring puckering analysis. This led to the following conclusions:

- For all reactions, except the reactions **oR3** and **oR7** and their two-water analogous reactions **tR8** and **tR9**, a similar

https://dx.doi.org/10.1021/acs.jpca.0c07244
J. Phys. Chem. A 2020, 124, 8978−8993

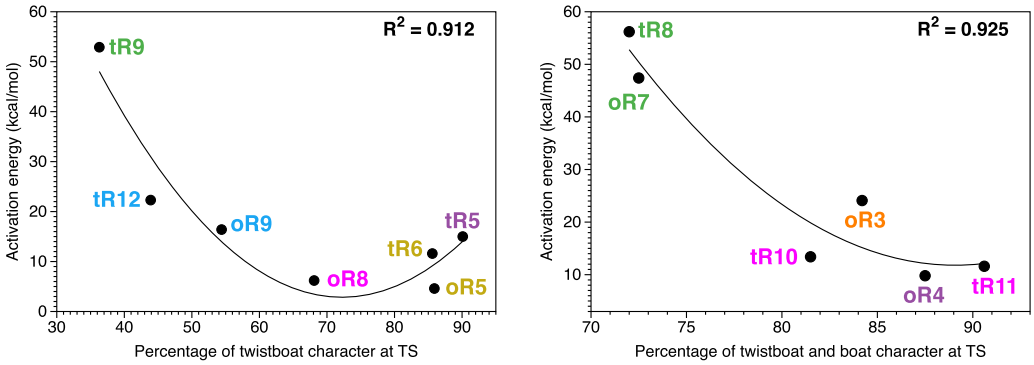

(a) Correlation between activation energy ΔE^a and percentage of twistboat character at the TS

(b) Correlation between activation energy ΔE^a and percentage of twistboat + boat characters at the TS

Figure 12. Correlations between the activation energy ΔE^a and percentage of twistboat and twistboat + boat characters at the TS.

curvature pattern in the chemical phases was found consisting of three curvature peaks. These peaks correspond to the major chemical events occurring during reaction, i.e., O−H cleavage, H−H formation, B(Al)−H cleavage, and O−B(Al) formation. In all cases, the O−H cleavage precedes the other chemical events. Interesting to note, the B(Al)−H cleavage spans over a range of peaks in a cost-effective fashion, resembling the metal−H bond cleavage.

- The local mode force constants of the O−H, H−H, B(Al)−H, and O−B(Al) calculated for R and TS complement the curvature data. The O−H cleavage process is characterized by a relative change in k^a between the R and TS of more than 75%. The same holds for the B(Al)−H cleavage. Furthermore, there is a correlation between the activation energy and the change in the charge separation for the cleaving O−H and B(Al)−H bonds going from the R to TS. For reactions with a larger change in the charge separation for the O−H bond corresponding to lower activation energies, electron-withdrawing substituents on the catalyst will reduce the activation barrier. On the other hand, for reactions with a smaller change in the charge separation for the B(Al)−H bond associated with lower activation energy, electron-donating substituents on the catalyst will further reduce the activation barrier. This provides useful guidelines for the modification of these catalysts.
- We observe moderate-to-strong H−H bonds at the TS for reactions leading to H_2 liberation. Most importantly, reactions without hydrogen release are characterized by a weak H−H bond (i.e., small k^a values) at the TS, thereby discarding any practical utilization of these catalysts for H_2 production. Trends between k^a(H−H) at the TS and activation energy reflect TS stabilization via dihydrogen bond formation. The stepwise cleavage of the O−B(Al) bond is indicated by moderately strong O−B(Al) bonds at the TS. The O−B(Al) bond strength of the byproduct provides insights into the regenerability of the catalyst. Accordingly, **oR8** and its two-water analogues **tR10** and **tR11** are the most promising candidates for catalyst regeneration.
- The driving force behind these reactions is the charge transfer between the catalyst and water. Oppositely charged H atoms of the catalyst and water participate in a dihydrogen interaction, which eventually leads to the release of a H_2 molecule. Except in **oR3** and **oR7** and their two-water analogous reactions **tR8** and **tR9**, the catalyst acts as a charge donor in the chemical phases. In reactions with no hydrogen release, the catalyst acts as a charge acceptor within the chemical phases. A molecular orbital analysis of **oR3** further confirmed the inability of the catalyst to act as a charge donor. The donation from the B−H sigma orbital to the O−H sigma antibonding orbital is extremely low, as revealed by the orbital interaction energies. As examined for $\mathbf{oR1}_{PCM}$, the overall charge-transfer mechanism in solution remains unaltered; however, it leads to a larger charge separation in the RC compared to the gas phase due to the presence of the polar medium.
- Conformational changes also contribute to the reaction mechanism and the activation barrier. In most cases, the reactions proceed through an intermediate six-membered ring. The puckering analysis suggests that the latter is predominantly of boat and twistboat characters. The puckering character of the TS correlates with the activation barrier. Two subsets of reactions were identified with lower barriers, favoring either 65−75% of the twistboat character or a high percentage of the boat and twistboat admixtures.

Inspired by the new insights, we are currently investigating how to best optimize these catalysts for efficient hydrogen evolution.

■ ASSOCIATED CONTENT

Supporting Information

The Supporting Information is available free of charge at https://pubs.acs.org/doi/10.1021/acs.jpca.0c07244.

Reaction schemes with original numbering, calculated bond lengths and local mode properties for selected bonds for all reactions; curvature decomposition into bond, angle, and dihedral components for all reactions; correlation analysis between the activation energy and change in charge separation for selected bonds for reactions **tR1**−**tR12**; local mode analysis of the B(Al)−H cleavage for reactions **tR1**−**tR12**; description of puckering coordinates; and coordinates of the stationary points of all reactions (PDF)

Reaction movies of all reactions (ZIP)

https://dx.doi.org/10.1021/acs.jpca.0c07244
J. Phys. Chem. A 2020, 124, 8978−8993

AUTHOR INFORMATION

Corresponding Author

Elfi Kraka − *Computational and Theoretical Chemistry Group (CATCO), Department of Chemistry, Southern Methodist University, Dallas, Texas 75275-0314, United States;* orcid.org/0000-0002-9658-5626; Email: ekraka@smu.edu

Authors

Sadisha Nanayakkara − *Computational and Theoretical Chemistry Group (CATCO), Department of Chemistry, Southern Methodist University, Dallas, Texas 75275-0314, United States*

Marek Freindorf − *Computational and Theoretical Chemistry Group (CATCO), Department of Chemistry, Southern Methodist University, Dallas, Texas 75275-0314, United States*

Yunwen Tao − *Computational and Theoretical Chemistry Group (CATCO), Department of Chemistry, Southern Methodist University, Dallas, Texas 75275-0314, United States*

Complete contact information is available at: https://pubs.acs.org/10.1021/acs.jpca.0c07244

Notes

The authors declare no competing financial interest.

ACKNOWLEDGMENTS

This work was supported by the National Science Foundation (grant CHE 1464906). The authors thank Southern Methodist University for providing excellent computational resources.

REFERENCES

(1) Hirscher, M.; Autrey, T.; Orimo, S.-I. Hydrogen Energy. *ChemPhysChem* **2019**, *20*, 1157.

(2) Tian, M.-W.; Yuen, H.-C.; Yan, S.-R.; Huang, W.-L. The Multiple Selections of Fostering Applications of Hydrogen Energy by Integrating Economic and Industrial Evaluation of Different Regions. *Int. J. Hydrogen Energy* **2019**, *44*, 29390−29398.

(3) Martin, A.; Agnoletti, M.-F.; Brangier, E. Users in the Design of Hydrogen Energy Systems: A Systematic Review. *Int. J. Hydrogen Energy* **2020**, *45*, 11889−11900.

(4) Maghami, M. R.; Hassani, R.; Gomes, C.; Hizam, H.; Othman, M. L.; Behmanesh, M. Hybrid Energy Management with respect to a Hydrogen Energy System and Demand Response. *Int. J. Hydrogen Energy* **2020**, *45*, 1499−1509.

(5) Dincer, I.; Acar, C. Review and Evaluation of Hydrogen Production Methods for Better Sustainability. *Int. J. Hydrogen Energy* **2015**, *40*, 11094−11111.

(6) Nikolaidis, P.; Poullikkas, A. A Comparative Overview of Hydrogen Production Processes. *Renewable Sustainable Energy Rev.* **2017**, *67*, 597−611.

(7) Zou, X.; Zhang, Y. Noble Metal-free Hydrogen Evolution Catalysts for Water Splitting. *Chem. Soc. Rev.* **2015**, *44*, 5148−5180.

(8) Zhang, J.; Wang, T.; Liu, P.; Liao, Z.; Liu, S.; Zhuang, X.; Chen, M.; Zschech, E.; Feng, X. Efficient Hydrogen Production on $MoNi_4$ Electrocatalysts with Fast Water Dissociation Kinetics. *Nat. Commun.* **2017**, *8*, No. 15437.

(9) Roger, I.; Shipman, M. A.; Symes, M. D. Earth-abundant Catalysts for Electrochemical and Photoelectrochemical Water Splitting. *Nat. Rev. Chem.* **2017**, *1*, No. 0003.

(10) Li, R. Latest Progress in Hydrogen Production from Solar Water Splitting via Photocatalysis, Photoelectrochemical, and Photovoltaic-photoelectrochemical Solutions. *Chin. J. Catal.* **2017**, *38*, 5−12.

(11) He, Z.; Fu, J.; Cheng, B.; Yu, J.; Cao, S. $Cu_2(OH)_2CO_3$ clusters: Novel Noble-metal-free Cocatalysts for Efficient Photocatalytic Hydrogen Production from Water Splitting. *Appl. Catal., B* **2017**, *205*, 104−111.

(12) Shinagawa, T.; Takanabe, K. Towards Versatile and Sustainable Hydrogen Production through Electrocatalytic Water Splitting: Electrolyte Engineering. *ChemSusChem* **2017**, *10*, 1318−1336.

(13) Duan, J.; Chen, S.; Zhao, C. Ultrathin Metal-organic Framework Array for Efficient Electrocatalytic Water Splitting. *Nat. Commun.* **2017**, *8*, No. 15341.

(14) Anantharaj, S.; Ede, S. R.; Sakthikumar, K.; Karthick, K.; Mishra, S.; Kundu, S. Recent Trends and Perspectives in Electrochemical Water Splitting with an Emphasis on Sulfide, Selenide, and Phosphide Catalysts of Fe, Co, and Ni: A Review. *ACS Catal.* **2016**, *6*, 8069−8097.

(15) Li, X.; Hao, X.; Abudula, A.; Guan, G. Nanostructured Catalysts for Electrochemical Water Splitting: Current State and Prospects. *J. Mater. Chem. A* **2016**, *4*, 11973−12000.

(16) Kalyva, A.; Vagia, E. C.; Konstandopoulos, A.; Srinivasa, A.; T-Raissi, A.; Muradov, N.; Kakosimos, K. Particle Model Investigation for the Thermochemical Steps of the Sulfur−ammonia Water Splitting Cycle. *Int. J. Hydrogen Energy* **2017**, *42*, 3621−3629.

(17) Zhai, S.; Rojas, J.; Ahlborg, N.; Lim, K.; Toney, M. F.; Jin, H.; Chueh, W. C.; Majumdar, A. The Use of Poly-cation Oxides to Lower the Temperature of Two-step Thermochemical Water Splitting. *Energy Environ. Sci.* **2018**, *11*, 2172−2178.

(18) Navlani-García, M.; Mori, K.; Kuwahara, Y.; Yamashita, H. Recent Strategies Targeting Efficient Hydrogen Production from Chemical Hydrogen Storage Materials over Carbon-supported Catalysts. *NPG Asia Mater.* **2018**, *10*, 277−292.

(19) Sandhya, K. S.; Remya, G. S.; Suresh, C. H. Intermolecular Dihydrogen Bonding in VI, VII, and VIII Group Octahedral Metal Hydride Complexes with Water. *J. Chem. Sci.* **2018**, *130*, No. 98.

(20) Echeverría, J.; Aullón, G.; Alvarez, S. Dihydrogen Intermolecular Contacts in Group 13 Compounds: H···H or E···H (E = B, Al, Ga) Interactions. *Dalton Trans.* **2017**, *46*, 2844−2854.

(21) Belkova, N. V.; Epstein, L. M.; Filippov, O. A.; Shubina, E. S. Hydrogen and Dihydrogen Bonds in the Reactions of Metal Hydrides. *Chem. Rev.* **2016**, *116*, 8545−8587.

(22) Custelcean, R.; Jackson, J. E. Dihydrogen Bonding: Structures, Energetics, and Dynamics. *Chem. Rev.* **2001**, *101*, 1963−1980.

(23) Nguyen, M. T.; Nguyen, V. S.; Matus, M. H.; Gopakumar, G.; Dixon, D. A. Molecular Mechanism for H_2 Release from BH_3NH_3, Including the Catalytic Role of the Lewis Acid BH_3. *J. Phys. Chem. A* **2007**, *111*, 679−690.

(24) Nguyen, V. S.; Matus, M. H.; Grant, D. J.; Nguyen, M. T.; Dixon, D. A. Computational Study of the Release of H_2 from Ammonia Borane Dimer $(BH_3NH_3)_2$ and its Ion Pair Isomers. *J. Phys. Chem. A* **2007**, *111*, 8844−8856.

(25) Nguyen, V. S.; Matus, M. H.; Ngan, V. T.; Nguyen, M. T.; Dixon, D. A. Theoretical Study of the Hydrogen Release from Ammonia Alane and the Catalytic Effect of Alane. *J. Phys. Chem. C* **2008**, *112*, 5662−5671.

(26) Gopakumar, G.; Nguyen, V. S.; Nguyen, M. T. Molecular Mechanism of Hydrogen Release Reactions: Topological Analysis using the Electron Localization Function. *J. Mol. Struct.: THEOCHEM* **2007**, *811*, 77−89.

(27) Sun, H.; Meng, J.; Jiao, L.; Cheng, F.; Chen, J. A Review of Transition-metal Boride/phosphide based Materials for Catalytic Hydrogen Generation from Hydrolysis of Boron-hydrides. *Inorg. Chem. Front.* **2018**, *5*, 760−772.

(28) Weiss, H. G.; Shapiro, I. Mechanism of the Hydrolysis of Diborane in the Vapor Phase. *J. Am. Chem. Soc.* **1953**, *75*, 1221−1224.

(29) Kawashima, Y.; Takeo, H.; Matsumura, C. Microwave Spectroscopic Detection of BFHOH and $BH(OH)_2$. *Chem. Phys. Lett.* **1978**, *57*, 145−147.

(30) Kawashima, Y.; Takeo, H.; Matsumura, C. Microwave Spectrum of Borinic Acid BH_2OH. *J. Chem. Phys.* **1981**, *74*, 5430−5435.

(31) Sakai, S. Theoretical Study of the Chemical Reactions of B2H6 with Lewis Bases (NH_3, PH_3, H_2O, and H_2S). *J. Phys. Chem. A* **1995**, *99*, 9080−9086.

(32) Swinnen, S.; Nguyen, V. S.; Sakai, S.; Nguyen, M. T. Calculations Suggest Facile Hydrogen Release from Water using Boranes and Alanes as Catalysts. *Chem. Phys. Lett.* **2009**, *472*, 175−180.

(33) Bader, R. *Atoms in Molecules: A Quantum Theory*; Clarendron Press: Oxford, 1995.
(34) Popelier, P. *Atoms in Molecules: An Introduction*; Prentice-Hall: Harlow, England, 2000.
(35) Becke, A. D.; Edgecombe, K. A Simple Measure of Electron Localization in Atomic and Molecular Systems. *J. Chem. Phys.* **1990**, *92*, 5397−5403.
(36) Zou, W.; Sexton, T.; Kraka, E.; Freindorf, M.; Cremer, D. A New Method for Describing the Mechanism of a Chemical Reaction Based on the Unified Reaction Valley Approach. *J. Chem. Theory Comput.* **2016**, *12*, 650−663.
(37) Kraka, E. Reaction Path Hamiltonian and the Unified Reaction Valley Approach. *WIREs: Comput. Mol. Sci.* **2011**, *1*, 531−556.
(38) Kraka, E.; Zou, W.; Tao, Y.; Freindorf, M. Exploring the Mechanism of Catalysis with the Unified Reaction Valley Approach (URVA) - A Review. *Catalysts* **2020**, *10*, No. 691.
(39) Tomasi, J.; Mennucci, B.; Cammi, R. Quantum Mechanical Continuum Solvation Models. *Chem. Rev.* **2005**, *105*, 2999−3094.
(40) Konkoli, Z.; Cremer, D. A New Way of Analyzing Vibrational Spectra. I. Derivation of Adiabatic Internal Modes. *Int. J. Quantum Chem.* **1998**, *67*, 1−9.
(41) Konkoli, Z.; Larsson, J. A.; Cremer, D. A New Way of Analyzing Vibrational Spectra. II. Comparison of Internal Mode Frequencies. *Int. J. Quantum Chem.* **1998**, *67*, 11−27.
(42) Konkoli, Z.; Cremer, D. A New Way of Analyzing Vibrational Spectra. III. Characterization of Normal Vibrational Modes in terms of Internal Vibrational Modes. *Int. J. Quantum Chem.* **1998**, *67*, 29−40.
(43) Konkoli, Z.; Larsson, J. A.; Cremer, D. A New Way of Analyzing Vibrational Spectra. IV. Application and Testing of Adiabatic Modes within the Concept of the Characterization of Normal Modes. *Int. J. Quantum Chem.* **1998**, *67*, 41−55.
(44) Zou, W.; Kalescky, R.; Kraka, E.; Cremer, D. Relating Normal Vibrational Modes to Local Vibrational Modes with the Help of an Adiabatic Connection Scheme. *J. Chem. Phys.* **2012**, *137*, No. 084114.
(45) Zou, W.; Cremer, D. Properties of Local Vibrational Modes: The Infrared Intensity. *Theor. Chem. Acc.* **2014**, *133*, No. 1451.
(46) Kraka, E.; Zou, W.; Tao, Y. Decoding Chemical Information from Vibrational Spectroscopy Data: Local Vibrational Mode Theory. *WIREs: Comput. Mol. Sci.* **2020**, *10*, No. e1480.
(47) Kraka, E.; Cremer, D. Computational Analysis of the Mechanism of Chemical Reactions in Terms of Reaction Phases: Hidden Intermediates and Hidden Transition States. *Acc. Chem. Res.* **2010**, *43*, 591−601.
(48) Cremer, D.; Kraka, E. From Molecular Vibrations to Bonding, Chemical Reactions, and Reaction Mechanism. *Curr. Org. Chem.* **2010**, *14*, 1524−1560.
(49) Cremer, D.; Larsson, J. A.; Kraka, E. In *Theoretical and Computational Chemistry*; Parkanyi, C., Ed.; Elsevier: Amsterdam, 1998; pp 259−327.
(50) Oomens, J.; Kraka, E.; Nguyen, M. K.; Morton, T. M. Structure, Vibrational Spectra, and Unimolecular Dissociation of Gaseous 1-Fluoro-1-phenethyl Cations. *J. Phys. Chem. A* **2008**, *112*, 10774−10783.
(51) Zou, W.; Kalescky, R.; Kraka, E.; Cremer, D. Relating Normal Vibrational Modes to Local Vibrational Modes: Benzene and Naphthalene. *J. Mol. Model.* **2013**, *19*, 2865−2877.
(52) Kalescky, R.; Kraka, E.; Cremer, D. Identification of the Strongest Bonds in Chemistry. *J. Phys. Chem. A* **2013**, *117*, 8981−8995.
(53) Kalescky, R.; Kraka, E.; Cremer, D. Description of Aromaticity with the Help of Vibrational Spectroscopy: Anthracene and Phenanthrene. *J. Phys. Chem. A* **2014**, *118*, 223−237.
(54) Kalescky, R.; Kraka, E.; Cremer, D. New Approach to Tolman's Electronic Parameter Based on Local Vibrational Modes. *Inorg. Chem.* **2014**, *53*, 478−495.
(55) Kalescky, R.; Kraka, E.; Cremer, D. Are Carbon-Halogen Double and Triple Bonds Possible. *Int. J. Quantum Chem.* **2014**, *114*, 1060−1072.
(56) Kalescky, R.; Zou, W.; Kraka, E.; Cremer, D. Quantitative Assessment of the Multiplicity of Carbon-Halogen Bonds: Carbenium and Halonium Ions with F, Cl, Br, and I. *J. Phys. Chem. A* **2014**, *118*, 1948−1963.
(57) Humason, A.; Zou, W.; Cremer, D. 11,11-Dimethyl-1,6-methano[10]annulene-An Annulene with an Ultralong CC Bond or a Fluxional Molecule. *J. Phys. Chem. A* **2015**, *119*, 1666−1682.
(58) Sethio, D.; Lawson Daku, L. M.; Hagemann, H.; Kraka, E. Quantitative Assessment of B−B−B, B−H_b−B, and B−H_t Bonds: From BH_3 to $B_{12}H_{12}^{2-}$. *ChemPhysChem* **2019**, *20*, 1967−1977.
(59) Makoś, M. Z.; Freindorf, M.; Sethio, D.; Kraka, E. New Insights into Fe−H_2 and Fe−H^- Bonding of a [NiFe] Hydrogenase Mimic − A Local Vibrational Mode Study. *Theor. Chem. Acc.* **2019**, *138*, No. 76.
(60) Makoś, M. Z.; Zou, W.; Freindorf, M.; Kraka, E. Metal-Ring Interactions in Actinide Sandwich Compounds: A Combined Normalized Elimination of the Small Component and Local Vibrational Mode Study. *Mol. Phys.* **2020**, No. e1768314.
(61) Verma, N.; Tao, Y.; Zou, W.; Chen, X.; Chen, X.; Freindorf, M.; Kraka, E. A Critical Evaluation of Vibrational Stark Effect (VSE) Probes with the Local Vibrational Mode Theory. *Sensors* **2020**, *20*, No. 2358.
(62) Freindorf, M.; Kraka, E. Critical Assessment of the FeC and CO Bond strength in Carboxymyoglobin - A QM/MM Local Vibrational Mode Study. *J. Mol. Model.* **2020**, *26*, No. 281.
(63) Kraka, E.; Freindorf, M. In *Topics in Organometallic Chemistry—New Directions in the Modeling of Organometallic Reactions*; Lledós, A.; Ujaque, G., Eds.; Springer: Berlin, Heidelberg, 2020; Vol. *67*, pp 1−43.
(64) Freindorf, M.; Kraka, E.; Cremer, D. A Comprehensive Analysis of Hydrogen Bond Interactions Based on Local Vibrational Modes. *Int. J. Quantum Chem.* **2012**, *112*, 3174−3187.
(65) Kalescky, R.; Zou, W.; Kraka, E.; Cremer, D. Local Vibrational Modes of the Water Dimer - Comparison of Theory and Experiment. *Chem. Phys. Lett.* **2012**, *554*, 243−247.
(66) Kalescky, R.; Kraka, E.; Cremer, D. Local Vibrational Modes of the Formic Acid Dimer - The Strength of the Double H-Bond. *Mol. Phys.* **2013**, *111*, 1497−1510.
(67) Kraka, E.; Freindorf, M.; Cremer, D. Chiral Discrimination by Vibrational Spectroscopy Utilizing Local Modes. *Chirality* **2013**, *25*, 185−196.
(68) Setiawan, D.; Kraka, E.; Cremer, D. Description of Pnicogen Bonding with the help of Vibrational Spectroscopy-The Missing Link Between Theory and Experiment. *Chem. Phys. Lett.* **2014**, *614*, 136−142.
(69) Setiawan, D.; Kraka, E.; Cremer, D. Strength of the Pnicogen Bond in Complexes Involving Group VA Elements N, P, and As. *J. Phys. Chem. A* **2015**, *119*, 1642−1656.
(70) Setiawan, D.; Kraka, E.; Cremer, D. Hidden Bond Anomalies: The Peculiar Case of the Fluorinated Amine Chalcogenides. *J. Phys. Chem. A* **2015**, *119*, 9541−9556.
(71) Kraka, E.; Setiawan, D.; Cremer, D. Re-Evaluation of the Bond Length-Bond Strength Rule: The Stronger Bond Is not Always the Shorter Bond. *J. Comput. Chem.* **2016**, *37*, 130−142.
(72) Zhang, X.; Dai, H.; Yan, H.; Zou, W.; Cremer, D. B-H π Interaction: A New Type of Nonclassical Hydrogen Bonding. *J. Am. Chem. Soc.* **2016**, *138*, 4334−4337.
(73) Setiawan, D.; Cremer, D. Super-Pnicogen Bonding in the Radical Anion of the Fluorophosphine Dimer. *Chem. Phys. Lett.* **2016**, *662*, 182−187.
(74) Oliveira, V.; Kraka, E.; Cremer, D. The Intrinsic Strength of the Halogen Bond: Electrostatic and Covalent Contributions Described by Coupled Cluster Theory. *Phys. Chem. Chem. Phys.* **2016**, *18*, 33031−33046.
(75) Oliveira, V.; Kraka, E.; Cremer, D. Quantitative Assessment of Halogen Bonding Utilizing Vibrational Spectroscopy. *Inorg. Chem.* **2017**, *56*, 488−502.
(76) Tao, Y.; Zou, W.; Jia, J.; Li, W.; Cremer, D. Different Ways of Hydrogen Bonding in Water - Why Does Warm Water Freeze Faster than Cold Water. *J. Chem. Theory Comput.* **2017**, *13*, 55−76.
(77) Oliveira, V.; Cremer, D. Transition from Metal-Ligand Bonding to Halogen Bonding Involving a Metal as Halogen Acceptor: A Study of Cu, Ag, Au, Pt, and Hg Complexes. *Chem. Phys. Lett.* **2017**, *681*, 56−63.

https://dx.doi.org/10.1021/acs.jpca.0c07244
J. Phys. Chem. A 2020, 124, 8978−8993

(78) Oliveira, V.; Cremer, D.; Kraka, E. The Many Facets of Chalcogen Bonding: Described by Vibrational Spectroscopy. *J. Phys. Chem. A* **2017**, *121*, 6845−6862.
(79) Oliveira, V.; Kraka, E. Systematic Coupled Cluster Study of Noncovalent Interactions Involving Halogens, Chalcogens, and Pnicogens. *J. Phys. Chem. A* **2017**, *121*, 9544−9556.
(80) Zou, W.; Zhang, X.; Dai, H.; Yan, H.; Cremer, D.; Kraka, E. Description of an Unusual Hydrogen Bond Between Carborane and a Phenyl Group. *J. Organomet. Chem.* **2018**, *865*, 114−127.
(81) Yannacone, S.; Oliveira, V.; Verma, N.; Kraka, E. A Continuum from Halogen Bonds to Covalent Bonds: Where Do λ^3 Iodanes Fit? *Inorganics* **2019**, *7*, No. 47.
(82) Oliveira, V. P.; Marcial, B. L.; Machado, F. B. C.; Kraka, E. Metal-Halogen Bonding Seen through the Eyes of Vibrational Spectroscopy. *Materials* **2020**, *13*, No. 55.
(83) Tao, Y.; Qiu, Y.; Zou, W.; Nanayakkara, S.; Yannacone, S.; Kraka, E. In Situ Assessment of Intrinsic Strength of X-I···OA Type Halogen Bonds in Molecular Crystals with Periodic Local Vibrational Mode Theory. *Molecules* **2020**, *25*, No. 1589.
(84) Yannacone, S.; Sethio, D.; Kraka, E. Quantitative Assessment of Intramolecular Hydrogen Bonds in Neutral Histidine. *Theor. Chem. Acc.* **2020**, *139*, No. 125.
(85) Martins, J.; Quintino, R. P.; Politi, J. R. S.; Sethio, D.; Gargano, R.; Kraka, E. Computational Analysis of Vibrational Frequencies and Rovibrational Spectroscopic Constants of Hydrogen Sulfide Dimer using MP2 and CCSD(T). *Spectrochim. Acta, Part A* **2020**, *239*, No. 118540.
(86) Zou, W.; Tao, Y.; Freindorf, M.; Cremer, D.; Kraka, E. Local Vibrational Force Constants - from the Assessment of Empirical Force Constants to the Description of Bonding in Large Systems. *Chem. Phys. Lett.* **2020**, *478*, No. 137337.
(87) Kraka, E.; Larsson, J. A.; Cremer, D. In *Computational Spectroscopy*; Grunenberg, J., Ed.; Wiley: New York, 2010; pp 105−149.
(88) Mayer, I. Bond Order and Valence Indices: A Personal Account. *J. Comput. Chem.* **2007**, *28*, 204−221.
(89) Cremer, D. In *Encyclopedia of Computational Chemistry*; Schleyer, P.; Allinger, N.; Clark, T.; Gasteiger, J.; Kollman, P.; Schaefer, H., III; Schreiner, P., Eds.; John Wiley & Sons: New York, 1998; pp 1706−1735.
(90) Cremer, D. In *Wiley Interdisciplinary Computational Molecular Science*; Schreiner, P.; Allen, W., Eds.; Wiley: New York, 2011; vol. *1*, pp 509−530.
(91) Ditchfield, R.; Hehre, W. J.; Pople, J. A. Self-Consistent Molecular-Orbital Methods. IX. An Extended Gaussian-Type Basis for Molecular-Orbital Studies of Organic Molecules. *J. Chem. Phys.* **1971**, *54*, 724−728.
(92) Hariharan, P. C.; Pople, J. A. The Influence of Polarization Functions on Molecular Orbital Hydrogenation Energies. *Theor. Chim. Acta* **1973**, *28*, 213−222.
(93) Clark, T.; Chandrasekhar, J.; Spitznagel, G. W.; Schleyer, P. V. R. Efficient Diffuse Function-augmented Basis sets for Anion Calculations. III. The 3-21+G Basis set for First-row Elements, Li-F. *J. Comput. Chem.* **1983**, *4*, 294−301.
(94) Castiñeira Reis, M.; López, C. S.; Kraka, E.; Cremer, D.; Faza, O. N. Rational Design in Catalysis: A Mechanistic Study of β-Hydride Eliminations in Gold(I) and Gold(III) Complexes Based on Features of the Reaction Valley. *Inorg. Chem.* **2016**, *55*, 8636−8645.
(95) Freindorf, M.; Sexton, T.; Kraka, E.; Cremer, D. The Mechanism of the Cycloaddition Reaction of 1,3-Dipole Molecules with Acetylene - An Investigation with the Unified Reaction Valley Approach. *Theor. Chem. Acc.* **2014**, *133*, No. 1423.
(96) López, C. S.; Faza, O. N.; Freindorf, M.; Kraka, E.; Cremer, D. Solving the Pericyclic-Pseudo pericyclic Puzzle in the Ring-Closure Reactions of 1,2,4,6-Heptatetraene Derivatives. *J. Org. Chem.* **2016**, *81*, 404−414.
(97) Sexton, T.; Kraka, E.; Cremer, D. Extraordinary Mechanism of the Diels-Alder Reaction: Investigation of Stereochemistry, Charge Transfer, Charge Polarization, and Biradicaloid Formation. *J. Phys. Chem. A* **2016**, *120*, 1097−1111.
(98) Neese, F. The ORCA Program System. *WIREs: Comput. Mol. Sci.* **2012**, *2*, 73−78.
(99) Riplinger, C.; Neese, F. An Efficient and Near Linear Scaling Pair Natural Orbital Based Local Coupled Cluster Method. *J. Chem. Phys.* **2013**, *138*, No. 034106.
(100) Fukui, K. The Path of Chemical Reactions - the IRC Approach. *Acc. Chem. Res.* **1981**, *14*, 363−368.
(101) Hratchian, H. P.; Kraka, E. Improved Predictor-Corrector Integrators For Evaluating Reaction Path Curvature. *J. Chem. Theory Comput.* **2013**, *9*, 1481−1488.
(102) Tao, Y.; Zou, W.; Cremer, D.; Kraka, E. *pURVA*; Southern Methodist University: Dallas, TX, 2020.
(103) Kraka, E.; Zou, W.; Filatov, M.; Gräfenstein, J.; Izotov, D.; Gauss, J.; He, Y.; Wu, A.; Konkoli, Z.; He, Z. et al. COLOGNE, 2020. http://www.smu.edu/catco (accessed July 07, 2020).
(104) Frisch, M. J.; Trucks, G. W.; Schlegel, H. B.; Scuseria, G. E.; Robb, M. A.; Cheeseman, J. R.; Scalmani, G.; Barone, V.; Petersson, G. A.; Nakatsuji, H. et al. *Gaussian 09*, revision D.01; Gaussian Inc.: Wallingford, CT, 2009.
(105) Weinhold, F.; Landis, C. R. *Valency and Bonding: A Natural Bond Orbital Donor−Acceptor Perspective*; Cambridge University Press: Cambridge, 2005.
(106) Reed, A. E.; Curtiss, L. A.; Weinhold, F. Intermolecular Interactions from a Natural Bond Orbital, Donor-acceptor Viewpoint. *Chem. Rev.* **1988**, *88*, 899−926.
(107) Freindorf, M.; Cremer, D.; Kraka, E. Gold(I)-Assisted Catalysis - A Comprehensive View on the [3,3]-Sigmatropic Rearrangement of Allyl Acetate. *Mol. Phys.* **2018**, *116*, 611−630.
(108) Patnaik, S.; Sadow, A. Interconverting Lanthanum Hydride and Borohydride Catalysts for C=O Reduction and C-O Bond Cleavage. *Angew. Chem., Int. Ed.* **2019**, *58*, 2505−2509.
(109) Wang, Z.; Patnaik, S.; Eedugurala, N.; Manzano, J.; Slowing, I. I.; Kobayashi, T.; Sadow, A.; Pruski, M. Sillica-supported Organo-lanthanum Catalysts for C-O Bond Cleavage in Epoxides. *J. Am. Chem. Soc.* **2020**, *142*, 2935−2947.
(110) Moussa, G.; Moury, R.; Demirci, U. B.; Şener, T.; Miele, P. Boron-based Hydrides for Chemical Hydrogen Storage. *Int. J. Energy Res.* **2013**, *37*, 825−842.
(111) Cremer, D.; Pople, J. A. General Definition of Ring Puckering Coordinates. *J. Am. Chem. Soc.* **1975**, *97*, 1354−1358.
(112) Cremer, D. Theoretical Determination of Molecular Structure and Conformation. XI. The Puckering of Oxolanes. *Isr. J. Chem.* **1983**, *23*, 72−84.
(113) Cremer, D.; Szabo, K. J. In *Conformational Behavior of Six-Membered Rings*; Juaristi, E., Ed.; Wiley-VCH: Weinheim, 1995; pp 59−135.

https://dx.doi.org/10.1021/acs.jpca.0c07244
J. Phys. Chem. A 2020, 124, 8978−8993